Microelectromechanical Systems (MEMS) Photoacoustic (PA) Detector of Terahertz (THz) Radiation for Chemical Sensing

THESIS

Richard A Newberry, 2nd Lieutenant, USAF

AFIT-ENG-14-M-58

**DEPARTMENT OF THE AIR FORCE
AIR UNIVERSITY**

AIR FORCE INSTITUTE OF TECHNOLOGY

Wright-Patterson Air Force Base, Ohio

AFIT-ENG-14-M-58

Microelectromechanical Systems (MEMS) photoacoustic (PA) detector of Terahertz (THz) radiation for chemical sensing

THESIS

Presented to the Faculty

Department of Electrical and Computer Engineering

Graduate School of Engineering and Management

Air Force Institute of Technology

Air University

Air Education and Training Command

In Partial Fulfillment of the Requirements for the

Degree of Master of Science in Electrical Engineering

Richard A Newberry, BS

2nd Lieutenant, USAF

March 2014

DISTRIBUTION STATEMENT A.
APPROVED FOR PUBLIC RELEASE; DISTRIBUTION UNLIMITED.

AFIT-ENG-14-M-58

Microelectromechanical Systems (MEMS) photoacoustic (PA) detector of Terahertz (THz) radiation for chemical sensing

Richard A Newberry, BS

2nd Lieutenant, USAF

Approved:

_____//signed//_____	14 Mar 2014
Ronald A. Coutu, Jr., PhD (Chairman)	Date
_____//signed//_____	26 Feb 2014
Derrick Langley, Major, USAF, PhD (Member)	Date
_____//signed//_____	26 Feb 2014
Ivan Medvedev, PhD (Member)	Date

Abstract

In this research effort, a Microelectromechanical system (MEMS) cantilever pressure sensor was designed, modeled, and fabricated to investigate the photoacoustic (PA) response of gases to terahertz (THz) radiation under low vacuum conditions. Previous efforts in this project were improved upon, to include lowering resting out-of-plane curvature to improve sensitivity of devices. Dimensional analysis is taken into consideration and altered dimensions also serve to boost sensitivity while improving fragility of devices. All devices were fabricated on silicon-on-insulator (SOI) wafers and tested in a custom designed THz vacuum chamber. Fabricated devices have a minimum normalized noise equivalent absorption (NNEA) coefficient of 4.28×10^{-10}, an improvement of 69% on prior 10μm devices.

Acknowledgments

Richard A. Newberry

Table of Contents

List of Figures

List of Tables

Microelectromechanical Systems (MEMS) photoacoustic (PA) detector of Terahertz (THz) radiation for chemical sensing
I. Introduction

1.1 Background

The process of photoacoustic (PA) wave generation is the effect of a sample absorbing photons and then generating a pressure wave as a result. This photoacoustic method can be used to study the chemical and physical properties of various samples, to include gas analysis, optical spectroscopy, or probing of optically thick samples [1]. The basic concept of photoacoustic detection are that when a sample absorbs light, a small portion of the molecules become excited and jump to higher energy levels. As they return back down to lower energy levels, they release heat and produce a pressure wave [1,2]. The resulting pressure wave can be detected with an appropriate sensor, such as a microphone used for a gaseous sample.

Terahertz (THz) radiation is electromagnetic radiation in the 300 Gigahertz – 0.3 Terahertz frequency range. It is chosen as the radiation source due to well documented chemical signatures in this regime and the penetrative properties of THz radiation [2]. The higher power radiation also provides for more spectral purity to receive a higher PA signal[4,5].

Currently, traditional microphones have fundamental limitations that make PA detection more difficult. The gap between the membrane surrounding the cantilever and the cantilever itself in optical microphones cannot be decreased below a certain limit, restraining the miniaturization of sensors [3]. This inability to decrease the gap size past a certain point will limit the signal range that is able to be measured by a sensor. Because

the goal of this project is to measure frequencies in the THz range, we require a sensor in the micron range. Also, the required resonant frequencies of cantilever microphones to best perform PA spectroscopy exist in the 1 – 1000 Hz frequency range. Because resonant frequency is a function of cantilever dimension, cantilevers must have a relatively high length to thickness ratio, approximately 700 – 1400, for thicknesses of either 10μm or 5μm respectively, which makes them fragile and difficult to fabricate and transport.

Trace gas analysis is a highly sought after capability since its applications are numerous in both civilian and military environments. However, current gas analysis is limited in portability due to the best current solution, which is large spectroscopy systems. By measuring this unique amount of energy released, it can be compared against a database of known elements and their collective spectral signatures and determine what substance that has just been irradiated in your spectroscopic test setup. Unfortunately, the path length of the radiation is a factor that must be accounted for and current spectroscopic setups can vary in length from 3 – 100 ft, making portable spectroscopy difficult [6,7].

1.2 Problem Statement

Modern spectroscopic methods involve large pieces of equipment and are generally limited to a laboratory setting due to their dependency upon the path length of the radiation to be sensed [8,9]. However, photoacoustic spectroscopy is independent of the absorption path of the radiation emitted from a sample, which makes it an ideal candidate for a portable spectroscopic system [4]. This research effort is being

undertaken to produce more sensitive microelectromechanical systems (MEMS) PA detectors of THz radiation with the goal of designing a smaller, portable spectroscopy system.

This research focuses on the fabrication of a MEMS cantilever sensor as the mechanism for PA spectroscopy. The effort will include producing a sensitive cantilever to be used as a microphone for PA detection. The deflection will be measured using a laser interferometer, and the two measurements will be compared.

The research question to be answered is how to design a MEMS cantilever to best perform PA spectroscopy. Investigative questions will detail answers on how to properly fabricate a sensitive cantilever, what dimensions for a cantilever are best for optimizing cantilever deflection, and how best to acquire spectroscopic data.

1.3 Scope, Limitations, Assumptions

This research focuses only on the fabrication of the cantilevers and their deflection due to the PA effect of a single gas, methyl cyanide. No other gases are used and all tests are performed using a single THz radiation source.

Another limitation to this current design is the leakage of heat in the system. As heat leaks away through thermal conduction from the cell walls or heat capacity of the gas, the pressure waves generated will begin to vary [4]. While this change can be modeled, its effect is considered negligible and not taken into consideration.

1.4 Methodology

The current method of collecting data involves placing the fabricated cantilevers in a stainless steel test chamber placed in a THz test setup at Wright State University. A

Virginia Diode Inc. THz radiation source is placed at one opening of the test chamber and a diode receives the resulting power signal. The deflection of the cantilever is currently measured with a laser interferometer that reflects a laser beam off of a gold (Au) stacked with Titanium (Ti) surface on the tip of the cantilever and passes through a series of apertures. It is required to use a Ti/Au stack since Au doesn't normally adhere well to silicon and Ti does. Ti was chosen as the adhesion layer instead of other metals, such as Chromium, to be consistent with the process follower previously developed by former students. As the laser deflects, the irises crop off portions of the laser and a separate diode measures the change in laser power. The changing laser power is compared to the THz signal to determine how accurately the cantilever deflection will match the THz signal.

1.5 Overview

Chapter two of this thesis will detail a literature review undertaken in support of this project. The literature review is conducted to determine similar research efforts along similar lines and to prevent duplication of efforts. It also provides a basis of understanding of the work accomplished in this field in order to best prepare for the research effort. Chapter three of this thesis describes the methodology used to perform the experiments. This chapter will include the specific experimental arrangement and all relevant information concerning the testing environment. It will include diagrams of the test arrangement along with the specifications of all equipment used so that future work wishing to replicate the research accomplished in this effort will be able to do so with more ease. Chapter four will present the data collected in this research effort. Chapter five will be an analysis of the data collected. Chapter six will be a conclusion of this

thesis and will include discussion of potential future works, changes to the research effort that could have been made in order to better acquire results, and an overview of the research effort.

II. Background

The literature review for this research effort includes topics covering spectroscopy, chemical sensing, and MEMS technologies involved in the design and fabrication of sensors for PA detection. First, the PA effect and its use for chemical sensing is discussed as are the various detection methods. This discussion includes the various MEMS technologies involved, such as thin films, piezoelectrics, and physical sensors.

2.1 Photoacoustic systems

The photoacoustic (PA) effect was first discovered by Bell, Tyndall, and Rontgen in 1880 and is the process of generating acoustic waves by irradiating a sample with photons [2,13,14]. Bell first published on this phenomenon when he discovered that modulated sun light incident on a thin disk generated sound waves [5]. However, this process has been largely without applications until 1968, when the prevalence of laser light sources dramatically increased. The concept of PA detection is simple. A sample is irradiated, which excites a portion of the molecules in the sample into higher energy bands [16,17]. These molecules fall back to ground energy states and this falling generates heat around the sample, which subsequently generates a pressure wave that propagates away from the source [1,2,18].

There are many variables that influence the sensitivity of PA sensing systems. One such variable is the noise which arises from electrical, Brownian, and vibrational sources. Typical Signal to Noise Ratio (SNR) in a PA system is given by

$$\text{SNR} = \frac{PA_{Signal}}{PA_{Noise}} \qquad\qquad (\,1\,)$$

where PA_{Signal} is the strength of the PA signal centered on an absorption line and PA_{Noise} is the strength of the PA signal when the system is tuned off an absorption line [6]. The noise floor of a PA signal is generally determined by taking the Root Mean Square (RMS) value of the signal over some sampling interval off an absorption line. There are some instances when the radiation frequency cannot be shifted adequately away from an absorption line, so the radiation source is either blocked or removed from the system [20,21,22].

The sensitivity of a system, α_{min} is a descriptor of the minimum absorption strength the PA system can detect and is defined as

$$\propto_{min} = \frac{\propto_{peak}}{SNR} \tag{2}$$

where α_{peak} is the value of the absorption coefficient measured divided by the SNR of the measurement. To achieve higher sensitivities, measured signals may be averaged over longer periods [7]. Lastly, since PA systems can vary immensely, it is important to have a standard value of sensitivity, and this is the normalized noise equivalent absorption (NNEA) coefficient and it is expressed as

$$NNEA = \propto_{min} P_0 \sqrt{T} \tag{3}$$

NNEA values allow for more accurate performance comparisons between PA systems by taking into account the sensitivity, α_{min}, the radiation power, P_0, and the PA signal averaging time, T [24,25].

2.2 MEMS Fabrication

There are many techniques and methods for fabricating MEMS devices; to include surface micromachining, bulk micromachining, and micromolding technologies.

7

MEMS are systems that can consist of electrical, mechanical, and optical components. For example, Figure 1 shows the first electrostatic MEMS device, a resonant gate transistor developed by Nathanson in the 1960s to filter or amplify electrical signals using the resonance of an electroplated cantilever [8].
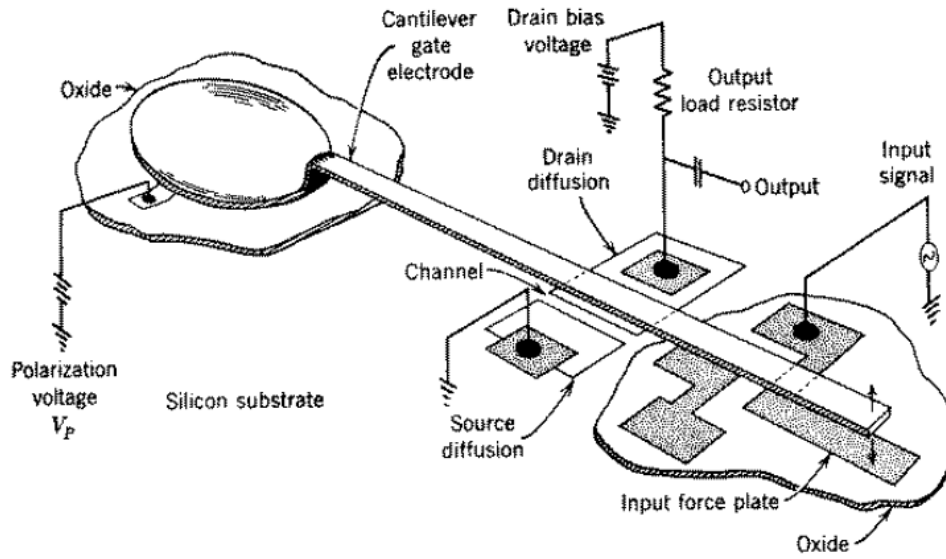
Figure 1. First MEMS device, a resonant gate transistor developed by Nathanson in the 1960s. This device was used to filter or amplify electrical signals using the resonance of a cantilever [9].

When an electrical signal is applied to the cantilever, the electrical attractive force actuates the cantilever and a detection circuit formed underneath the beam detects the filtered or amplified signal generated by the vibration.

2.2.1 Surface micromachining

Surface micromachining is the process of forming structural layers on a sacrificial structure, which is a structure whose sole purpose is for layers to be built on top of it, and

removal of the sacrificial layer, leaving behind a desired structure, typically a mechanical

layer. This technique can be used to create structures on top of substrate materials.
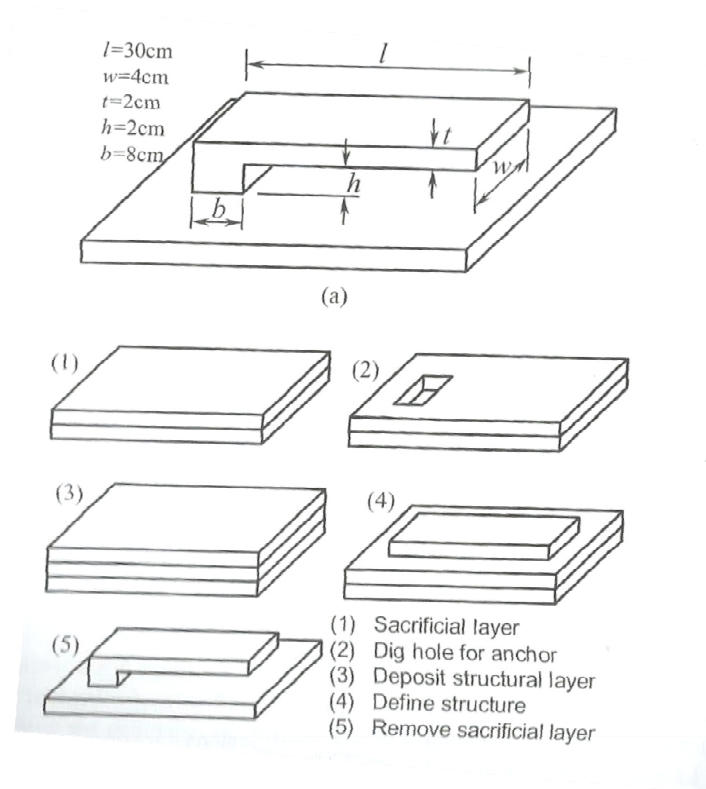
Figure 2. Creating of a cantilever structure via surface micromachining. Shown is the sacrificial layer being deposited in step (1), an anchor being dug in step (2), and the mechanical layer being deposited in step (3). After the device is shaped, removal of the sacrificial layer in step (5) is how the cantilever is released [8].

In Figure 2, a sacrificial layer is deposited in step (1). An anchor is "dug" into it and a

mechanical layer is layered on top. After shaping the structure, the sacrificial layer is

removed and your mechanical layer is left as your final structure. By using photoresist as

the sacrificial layer, a gold tip may be deposited onto devices without having to coat the

entire structure.

2.2.2 Bulk micromachining

.   Bulk micromachining is the process of creating structures out of the substrate material itself. This is done by the direct machining of the bulk material through chemical or physical means. It is relatively simpler than surface micromachining, as it generally requires fewer masks. The primary method of bulk micromachining in this research effort is through etching.

2.2.2.1 Wet Etching

Wet etching uses a wet etchant to form structures by removing undesired layers or portions of layers under a structure. Wet etchants are generally categorized as having isotropic or anisotropic etch profiles.

Isotropic etchants have the characteristic of etching in all directions at nearly the same rate. Isotropic etching of bulk silicon and a layer on a substrate is illustrated in Figure 3.
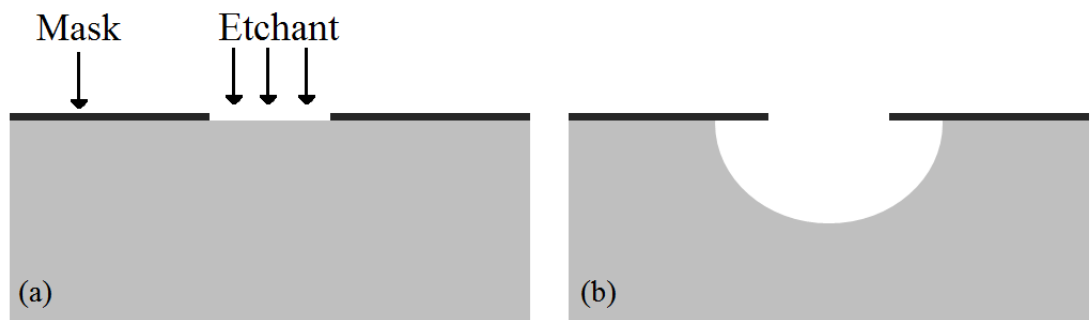
Figure 3. Isotropic etching profile. A mask is applied to the surface of the substrate in (a) and as the etchant reacts with the exposed substrate, it etches equally in all directions. This results in the undercutting of the masking material shown in (b).

In Figure 3a, a channel is etched into bulk silicon with an isotropic etchant, and as a result, the masking layer is undercut. The degree and severity of the undercut can be

influenced by the type of etchant, temperature, and agitation. Etchants can be selected based upon many criteria, to include the material to be etched, the masking material, and other materials that may be exposed to the etchant.

Anisotropic etchants are those that etch much more quickly in one direction than others. For example, potassium hydroxide (KOH) can be used to anisotropically etch a (100) bulk silicon wafer since its etch rate in the <111> direction is nearly 0 compared to other directions [8]. Figure 4 shows how KOH etches aggressively in the <100> direction but very slowly in the <111> direction.
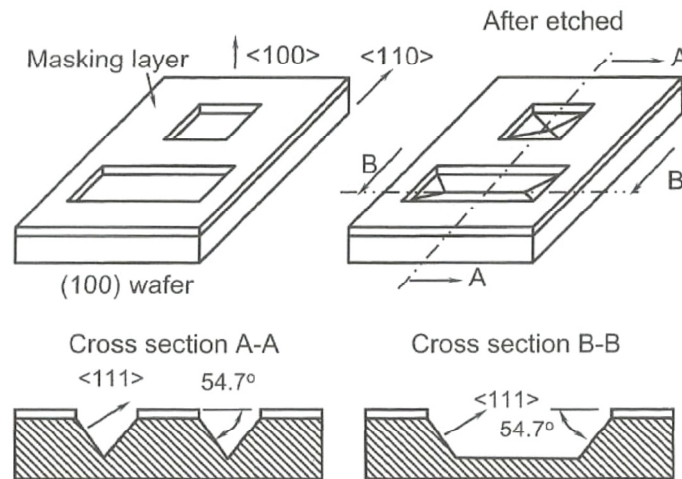
Figure 4. Anisotropic etching results in 'V' grooves due to the etchant reacting almost entirely in the <100> direction [8].

This type of anisotropic etch can be used to form 'V' grooves into a sample or in any application where a directional etch is desired [10].

2.2.2.2 Dry Etching

Dry etching is performed with dry etchants that are typically categorized into two categories, gas vapors or plasmas. Gas vapors are generally selected due to their

chemistry and selective reactions. For instance, vaporized hydrofluoric acid (HF) etches silicon dioxide much more quickly than bulk silicon, and HF is commonly used to etch away SiO_2 that is commonly applied as sacrificial layers while the silicon acts as an etch stop.

There are many forms of plasma etching, the most basic of which is that done by inert ions in plasma. These inert ions are accelerated into a layer and the kinetic energy of the ion removes a small piece of the layer in the resulting collision. This principle, known as sputtering is a physical destruction of a target [8]. The inert ion may be replaced with a reactive ion, such as sulfur hexafluoride (SF_6). However, it is only reactive to certain materials, based on chemistry, such as silicon. This process is known as reactive ion etching (RIE) and is an isotropic etch.

A specialized derivation of RIE exists and is known as deep reactive ion etching (DRIE). This specialized process allows for high-aspect ratio silicon structures [11]. This is considered a silicon tool since it is based upon SF_6. This process involves a series of shallow RIE etches and can provide aspect ratios of up to 30:1 and sidewall angles of 90 $\pm 2º$ [27,31]. Figure 5 demonstrates the DRIE process.
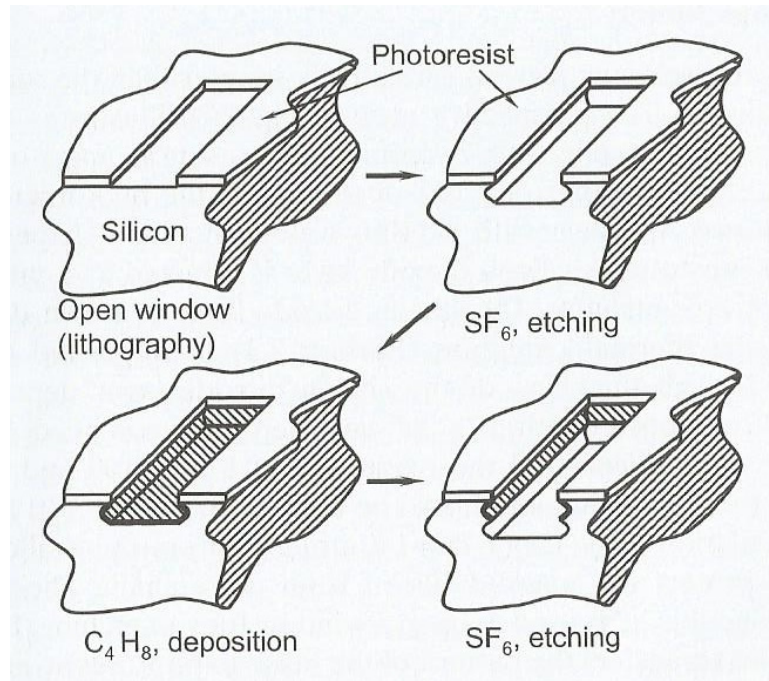
Figure 5. Mechanics of DRIE, which uses SF_6 as the etchant to perform a series of RIE etches into a silicon substrate. While high aspect ratios can be achieved, the sidewalls of a DRIE etch are scalloped due to the isotropic nature of the RIE etch [8].

Combined, these techniques allow for two general styles of MEMS fabrication, surface and bulk micromachining. Simply stated, surface micromachining involves depositing, patterning, and etching subsequent layers of thin films. Bulk micromachining differs in that the substrate, typically single crystalline silicon, is patterned and shaped to form a structure.

2.2.3 Micromolding

Micromolding is the process of creating MEMS structures through the use of a mold for casting of polymers.

UV exposure

SU-8

Silicon Substrate

(a)

Flexible mold

Mold master

(d)

Rigid mold

SU-8

Silicon Substrate

(b)

Polymer

Flexible mold

(e)

Mold master

SU-8

Silicon Substrate

(c)

Final structure

Polymer

(f)
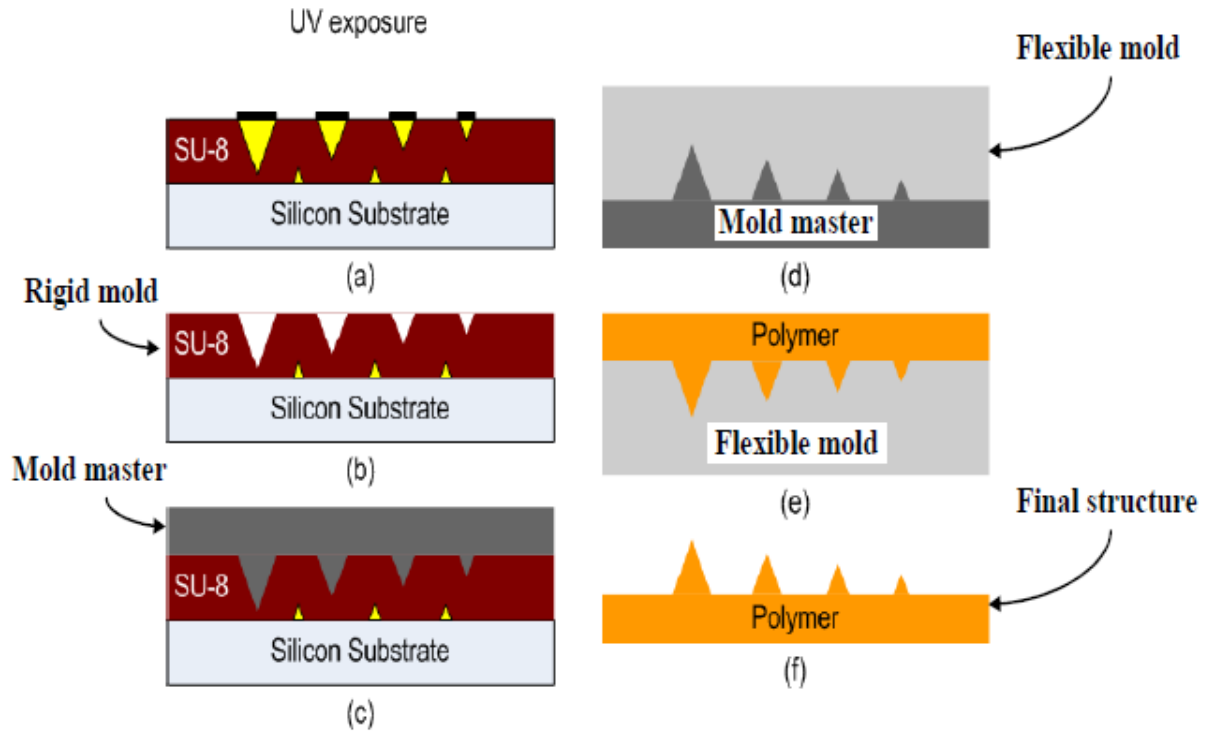
Figure 6. Micromolding process shows how a mold is created in (b) which is used to create a mold master in (c). This mold master is used to create flexible molds (d) which are used to shape polymers into your desired structures (f) [12].

In this process, shown in Figure 6, a rigid mold is fabricated out of SU-8 to form a negative of our desired structure. This rigid mold is used to produce a mold master from a suitable material, that is dependent upon desired material properties. The mold master is then used to create a flexible mold that is a copy of the original model. It is best to choose a material with a low modulus and low surface energy to allow for best results in casting structures. Polymer microstructures are then fabricated from the final flexible mold [12].

2.2.4 Silicon-on-insulator (SOI) Processing

SOI processing is unique in that the bulk substrate is a combination of materials, an insulator in between silicon, that have been pre-deposited prior to processing. In the

case of this research effort, bulk silicon was deposited with approximately 1μm of silicon dioxide and 10μm of silicon on top of that. Fabrication of the cantilever is done via bulk micromachining of the top, silicon device layer through DRIE. However, it can be considered surface micromachining since the silicon dioxide is used as a sacrificial layer for the mechanical layer.

SOI wafers may be produced by several methods, to include separation by implantation of oxygen (SIMOX) or through wafer bonding [13]. Figure 7 shows the process of SIMOX.
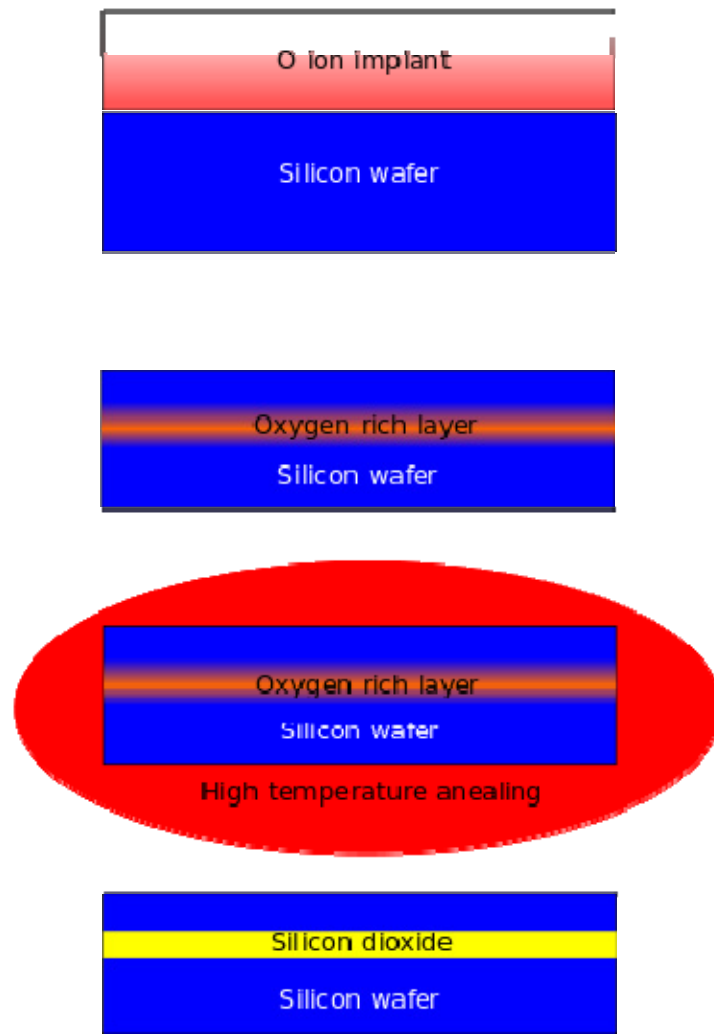
Figure 7. Separation by implantation of oxygen (SIMOX) is a process of creating silicon-on-insulator (SOI) wafers. Oxygen ions are implanted into a silicon wafer and an anneal is used to combine these oxygen atoms with the surrounding silicon. The result is a layer of silicon dioxide within the wafer. The depth of the insulating layer is dependent upon the power used during ion implantation [14].

First, an oxygen ion beam is used to implant oxygen within the silicon layer. Then a high

temperature anneal is used to anneal the oxygen which both helps to grow silicon dioxide

and helps to form the crystalline structure of the silicon dioxide.

16

It is also possible to first grow the oxide then apply a top layer of silicon as shown in Figure 8.

.
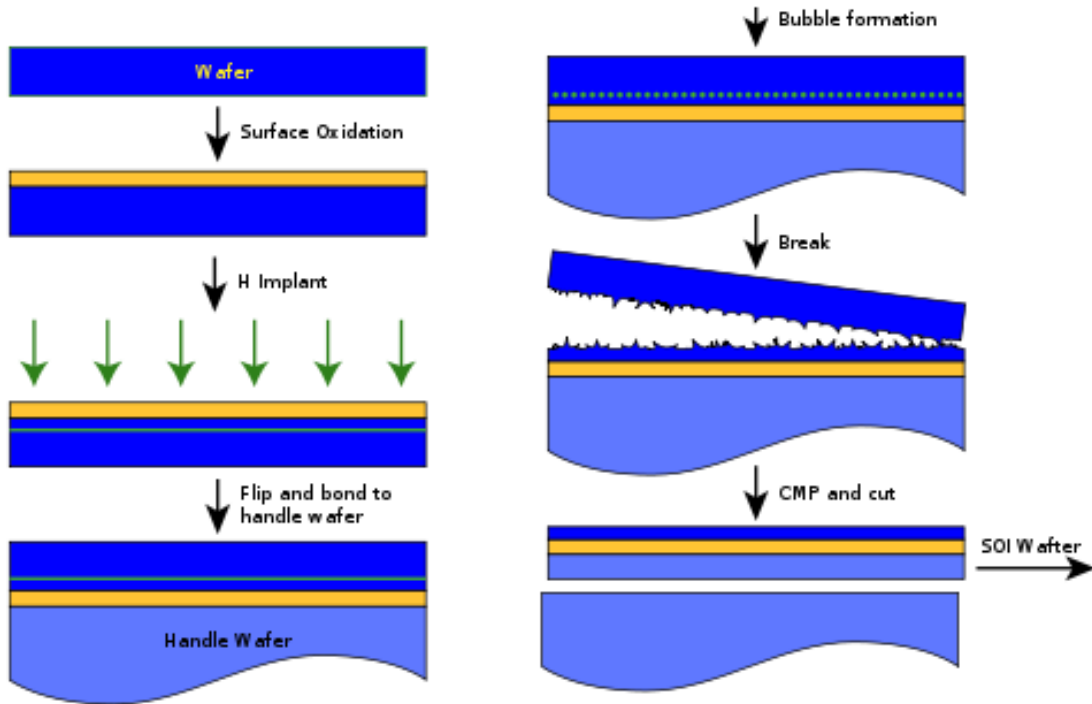
Figure 8. Creation of silicon-on-insulator (SOI) wafers through wafer bonding. An oxide is grown at the surface of a silicon substrate, and a second silicon wafer is flip bonded onto the oxide. The top wafer is cut along bubbles in the silicon created through "controlled exfoliation" and then smoothed through chemical mechanical polishing (CMP). This technique, known as the "Smart Cut" process was developed by Soitec [34,35].

This process shown is done through wafer bonding, that is, bonding two silicon wafers and then using chemical and mechanical polishing (CMP) to smooth down the top silicon substrate. In this process, developed by Soitec [15], an oxidation layer is grown onto a silicon substrate and a second wafer is bonded to the surface. The second wafer is then

brought to the desired thickness through "controlled exfoliation" which is the breaking of the second wafer along a line of "bubbles" implanted into the top wafer [14].

SOI processing is the chosen method for cantilever fabrication in this research effort as the included buried oxide acts as the sacrificial layer required for forming mechanical layers on substrate silicon.

2.3 PA sensing element

In order to best detect PA signals, a microphone is required as a sensing element. Several research groups have tackled the photoacoustic analysis of gasses and other materials using fabricated cantilever, bridges, and membrane microphones. The first model of sensing elements were Helmholtz resonators [16]. This type of sensor is an open and adjoining neck. The air in the open cavity oscillates while the air in the neck acts as a spring to dampen the oscillations [16]. The resulting wave generated can be measured through the output of the neck. While simple, this setup does not generate enough sensitivity in order to perform accurate spectroscopy.

There has been success using a capacitive microphone, which is a flexible membrane acting as the sensor [17]. This membrane deforms due to the pressure variations in the gas sample and this deformation is measured via an interferometer. However, since the entire membrane is strained and has to stretch radially, it lacks very high sensitivities, such as those desired by this research effort, cannot be achieved [17].

A more complicated method, but the preferred method of choice for this research is a MEMS cantilever as the sensing element due to the capability to achieve higher sensitivities. Cantilever designs can be used in a wide range of sensor applications.

18

Cantilever feature dimensions can be on the millimeter scale all the way down to the nanometer scale depending on the application. For sensor applications, there are many ways to extract information based on the cantilever behavior. Changes in the cantilever resonant frequency, tip amplitude displacement, piezoelectric signal, or combinations of these signal behaviors can be used to infer information about changes to the environment. A micromachined, silicon cantilever used as the sensing element can achieve higher sensitivities than traditional methods [18]. A cantilever also has the benefit of being a mechanical structure, which has a series of natural, vibrational modes or resonant frequencies. By knowing which particular samples that are desired to be sensed, the cantilever can be designed to have a resonant frequency around the frequencies expected to achieve through the PA spectroscopic techniques. These cantilevers may be measured through a piezoelectric layer applied to the surface of the beam or through an optical measurement, such as a Michelson type interferometer or other variations.

De Paula *et al*. reported an early optical microphone for PA spectroscopy of solids where they optically measured the deflection of a pellicle placed over a duct outside a PA chamber [19]. The designed sensor was a 25 μm thick Mylar droplet shaped pellicle cantilever that was mirrored and 13 mm long, 2.5 mm wide at the tip, and tapered down to the anchor of 1.5 mm wide. A 1,000 W Xeon lamp was used as the radiation source which was then filtered using band pass slits 10 nm across. PA spectra of a blackened Teflon surface was collected at a modulation frequency of 17 Hz, sweeping at a rate of 50nm/min across a spectrum of approximately 300 – 900 nm wavelengths, and with a time constant of 3 s [19]. Modulation frequency scans of the radiation source showed the

maximum PA signal was achieved at 17 Hz due to the long, flexible design of the Mylar pellicle sensor.

Ledermann *et al.* [20] fabricated piezoelectric acoustic sensors out of bridge and cantilever structures for CO_2 detection. Samples were made out of a solid silicon wafer that was backside etched to control the device layer thicknesses, which ranged from 5 - 20 μm. Figure 9 (a) is an example of the one of the $2 \times 2 \times 0.017$ mm^3 (length × width × thickness) fabricated cantilever designs with a 5 μm gap around the edge of the beam. A pulsed incandescent lamp was used in the test chamber as the radiation source. The photoacoustic results shown in Figure 9 (b), 200-1,300 μV was the measurable generated voltage from the lead zirconate titanate (PZT) material on the cantilever design depending on the CO_2 concentration. The cantilever design by far outperformed the bridge sensor by almost a factor of two; with the cantilever producing 170 mV/Pa and the bridge sensor producing 93 mV/Pa.
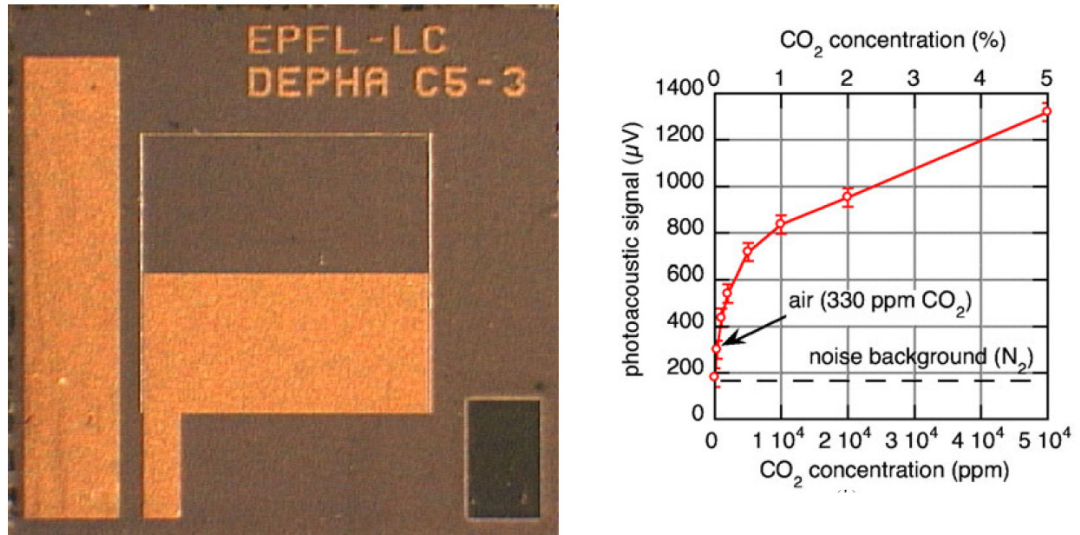
Figure 9. (a) 2x2x0.017mm cantilever sensor fabricated by Ledermann *et al.* and (b) PA results for CO_2 [20]

For the fabrication process, Ledermann *et al.* used a 1 μm thick thermal oxide under the bottom electrode to compensate for stress in the cantilever that built up as the additional layers were added [20]. The TiO$_2$/Ti and Pt bottom electrode materials along with a {100}-oriented PbTiO$_3$ seed layer was used to improve the crystal formation of the deposited PZT films. The seed layer established the desired orientation and texture for the preferential crystal formation of the PZT. Deposited by chemical solution deposition (sol-gel), a 1 μm thick PZT film was used as the piezoelectric material layer. During the PZT spin on deposition process, samples went through multiple bakes at 350 °C and a final anneal at 650 °C under a flow of oxygen. X-ray diffraction (XRD) analysis was performed on the annealed PZT films which showed good film crystallinity. After the top Cr/Au contact layer was in place, the PZT film was hot poled at 150 °C for 10 minutes with a 200 kV/cm applied electric field, which is about a 20 V applied potential [20].

Kuusela *et al.* has made recent progress in making a small photoacoustic trace gas detection chamber with cantilever sensor and laser interferometer measurements [1,6]. In 2009, they tested six different gases in their chamber with a 10 μm thick silicon cantilever that was 3×1.5×0.01 mm^3 with 5 μm gap around edge of the cantilever. In the tests, three different LED sources centered at 3.4, 4.2, and 7.0 μm wavelengths were used to excite the gaseous species that had absorption lines within those wavelengths. The lowest detection limit achieved was 6 ppm for propane with a 1 s sample integration time. Experiments were performed at atmospheric pressure (760 Torr) and the gas species were diluted with nitrogen to control the concentration [6,40]. LED's offered a compact, low cost option for the for PA excitation source. The broad emitted power spectrum of the

LED sources spanned multiple absorption lines of the gasses under investigation. Dips in the spectral output power of the 7 μm wavelength LED was due to the absorption lines of water. Due to the broad spectral output of the LED's, this system design could only perform chemical detection for a limited number of gases.

A benefit in fabricating optically detected cantilevers is that it limits the number of layers required to fabricate a cantilever microphone so it removes the two electrode and piezoelectric layers. Also, cantilever microphones whose displacement is measured with Michelson-type laser interferometers have so far achieved the highest sensitivities in PA systems [6,41,42]. However, this sensitivity is closely controlled by the fabrication process and properties of the silicon. For instance, the work done by Sievila *et al.* characterizes the sensitivities of the cantilevers as they relate to the deflection of the cantilever out of plane. After the cantilevers are fabricated, the curvature out of plane is measured interferometrically. The angle of deflection shown in Figure 10 is reported to vary from 10^{-3} rad to 10^{-2} rad [21].
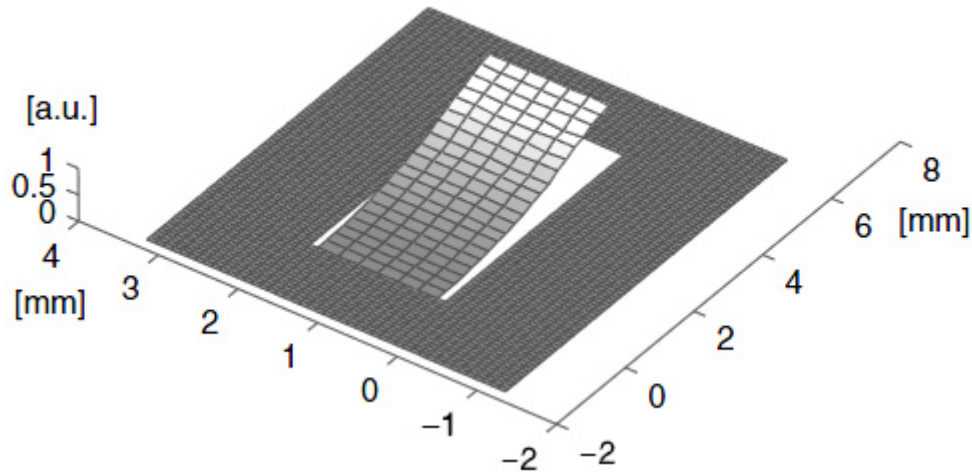
Figure 10. Cantilever deflection at rest of the cantilever fabricated by Sievila *et al*. This shows that without external stimuli, the cantilever is bent out of plane due to an internal stress gradient along the length of the cantilever. The displacement is not to scale [21].

This bending out of plane allows for a larger gap between the cantilever and membrane, which limits the damping of the cantilever from the gas and ultimately lowers sensitivity. However, these cantilevers were masked for etching by thermally growing an oxide onto the surface, which diffuses dopants further into the silicon resulting in internal stress [22]. It has been shown that depositing an through plasma enhanced chemical vapor deposition (PECVD) and a subsequent anneal can lower the released curvature to having radii of curvatures from 4.5 m to 15 m [22].

As mentioned earlier, the gap between the cantilever gap and membrane is crucial as to prevent leakage of gases and proper damping of the cantilever system. This gap is dependent upon the resolution of the patterning and the etch performed to release the cantilever. The release process performed by Sievila *et al.* is a wet etch. The etchant used

is tetramethylammonium hydroxide (TMAH) which has an isotropic etch profile. This results in a larger gap around the corner of the cantilever as shown in Figure 11 [23].
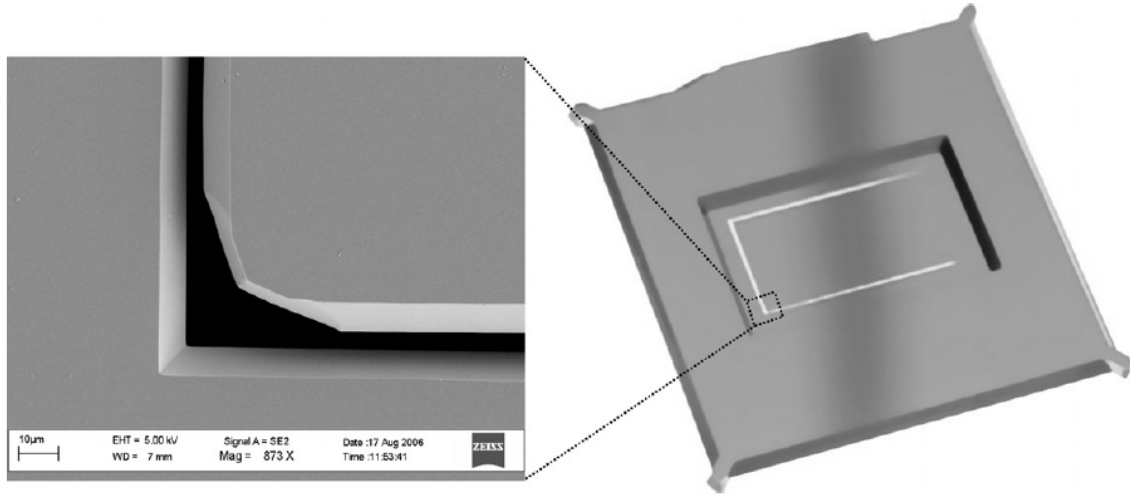
Figure 11. SEM image of rounded corner of cantilever fabricated by Sievila *et al*. This rounded corner is due to the isotropic etch of tetramethylammonium hydroxide (TMAH) which was used to release the device. This rounded corner increases the gap around the corner and is a source of sensitivity loss [44,45].

This rounded corner is also a source of gas leakage and a loss of sensitivity in the PA system due to the membrane gap around the corner increasing from approximately 3μm along the edge of the beam to approximately 20 μm at the corner.

The process for designing a piezoelectric cantilever is similar to an optically detected cantilever with the inclusion of two electrodes sandwiching a piezoelectric material, such a lead zirconate titanate (PZT) or zinc oxide (ZnO) [35,46,47,48]. Figure 12 shows the fabrication process for a piezoelectric cantilever.
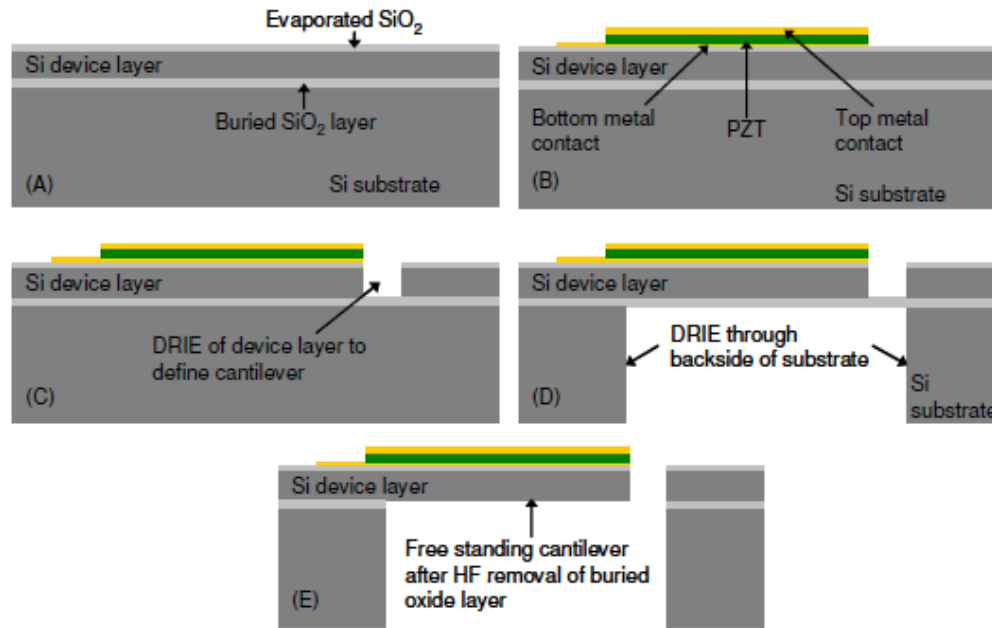
Figure 12. Piezoelectric cantilever fabrication process[27]. The additional layers applied to the surface of the cantilever will generate an electric potential between the top and bottom metal contacts when the cantilever is strained. This could yield in a more portable system, but the added layers could hinder cantilever motion [49,50].

This process shows PZT as the piezoelectric layer, but success has been reported using ZnO as well [35,51,52,53,54,55]. Figure 13 shows a fabricated ZnO cantilever.
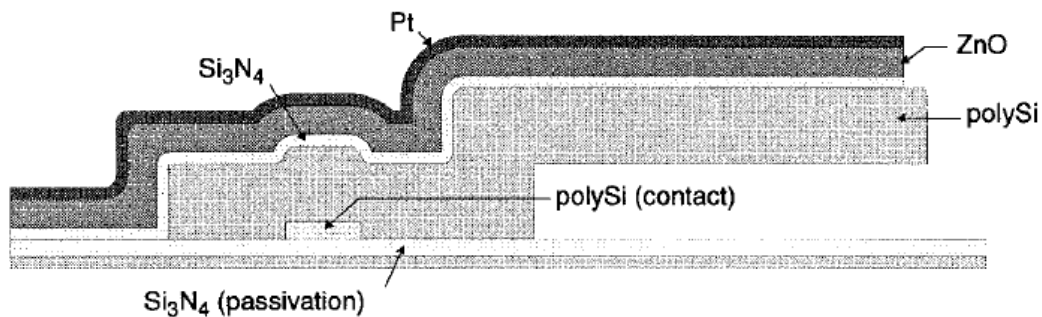
Figure 13. Cross section of zinc oxide (ZnO) cantilever. ZnO has had reported success as the piezoelectric layer in fabricating cantilever sensors [35,54].

However, as stated above, adding piezoelectric layers to a cantilever microphone comes with tradeoffs. For not needing an external interferometer, a loss of sensitivity is incurred [49,50,56,57].

2.4 Cantilever motion

Cantilever bending in an underdamped system can be expressed through analytical models where the tip displacement A is given by

$$A(\omega) = \frac{F}{m\sqrt{(\omega_0^2 - \omega^2)^2 + 4(\frac{1}{\tau})^2 \omega^2}} \cong \frac{F\tau}{2m\omega} \tag{4}$$

where τ is the time constant, m is the mass of the cantilever, F is the applied force, ω is angular frequency, and ω_0 the angular resonant frequency [8]. An examination of this equation reveals that an increase in time constant, reduction in mass, and reduction in resonant frequency will allow for larger deflections for a given force. A cantilever's resonant frequency f_0 is described by

$$f_0 = \frac{1}{2\pi} \sqrt{\frac{k}{m_{eff}}} \tag{5}$$

where k is the sprint constant and m_{eff} is the effective mass of the cantilever [8]. Effective mass of a cantilever takes into account how easily the cantilever is accelerated due to spring constant and can be calculated using Rayleigh's method through the conservation of energy[28]. Using this method, it is shown that the effective mass of a cantilever is described by

$$m_{eff} = \frac{104}{405} \rho whL \approx \frac{1}{4} \rho whL \tag{6}$$

where ρ is the density of the material, L is the length, w is the width, and h is the thickness of the cantilever.

The spring constant, k, of a cantilever beam can be described by

$$k = \frac{2}{3} E_\gamma w \left(\frac{h}{L}\right)^3 \qquad (7)$$

where E_γ is the Young's modulus of the material. Often, cantilevers are not perfectly flat due to the imperfect nature of SOI and the internal stress that is built when annealing the buried oxide which expands differently than the silicon layer on top. This results in a curvature to the cantilever. By measuring the radius of curvature, the internal stress gradient, $\Delta\sigma$ can be measured through the use of Stoney's equation.

$$\frac{1}{R} = \frac{6\,(1-v)\Delta\sigma}{E_\gamma d^2} \qquad (8)$$

Where R is the radius of curvature, E_γ is the Young's Modulus for the cantilever material, in this case, silicon, v is Poisson's ratio corresponding to the crystal orientation of the bending cantilever, and d is the thickness of the beam.

2.5 Finite Element Method (FEM)

Finite element method is a problem solving method that is used to find approximate solutions to a field problem[29]. Field problems, which are described through differential equations, attempt to determine "spatial distribution of one or more dependent variables" [35,59]. FEM takes a device or area and divides it into finite elements, which together, represent the entire physical structures. The boundaries between elements are called nodes. The arrangement of elements within the structure is defined as the mesh. The mesh created is "represented by a system of algebraic equations to be solved for unknowns at the nodes"[29]. Performed in a piecewise fashion, approximate solutions of the structure are calculated element by element. The accuracy of the solution can be increased by increasing the number of elements in the structure. FEM

27

simulations can be used to model the behavior of a particular device which is constrained

by material properties, boundary conditions, and applied stimuli.

III. Methodology

Photoacoustic spectroscopy can be broken into two main components, the generation and sensing of pressure waves. This research effort focuses primarily on the sensing aspect, which is accomplished by a designed and fabricated cantilever which is housed by a stainless steel photoacoustic chamber. This chapter details the efforts in the design and process of creating the testing fixtures.

3.1 Wave Generation

The gas species chosen for this research effort is Methyl Cyanide (CH_3CN). This gas is chosen due to it being well documented in the THz regime and having absorption lines over a wide range of frequencies, from $0.018 - 1.8065$ THz. Figure 14 shows the absorption spectrum for Methyl Cyanide as characterized by NASA's Jet Propulsion Labs (JPL) [24].
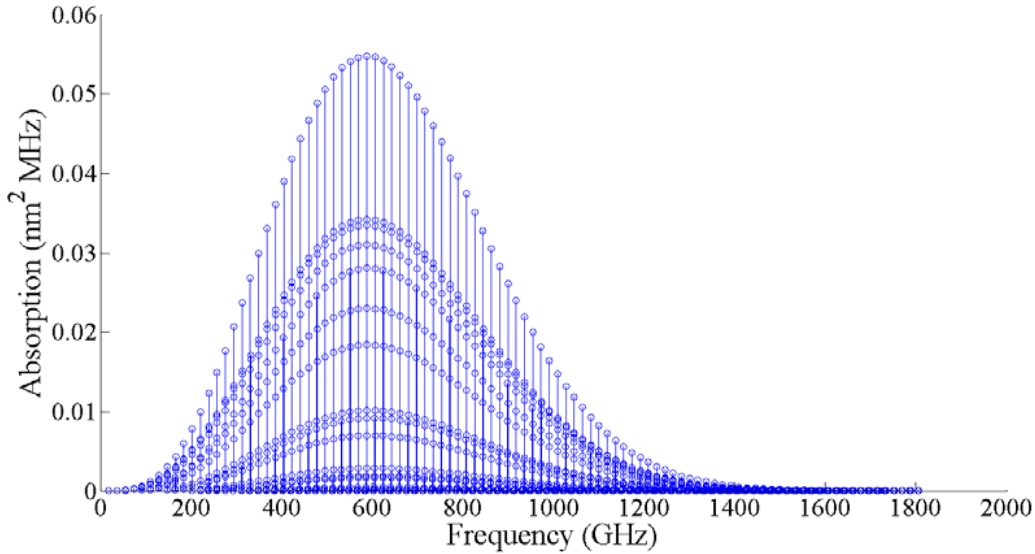
Figure 14. Absorption spectrum for Methyl Cyanide as characterized by NASA's Jet Propulsion Labs. Methyl Cyanide has absorption lines from $0.018 - 1.8065$ THz [24].

This graph displays the entire absorption spectrum for Methyl Cyanide, which spans 1.7885 THz. For the purposes of this research effort, only a fraction of this spectrum is required. Figure 15 shows the absorption lines of Methyl Cyanide as characterized by prior students in this research project.
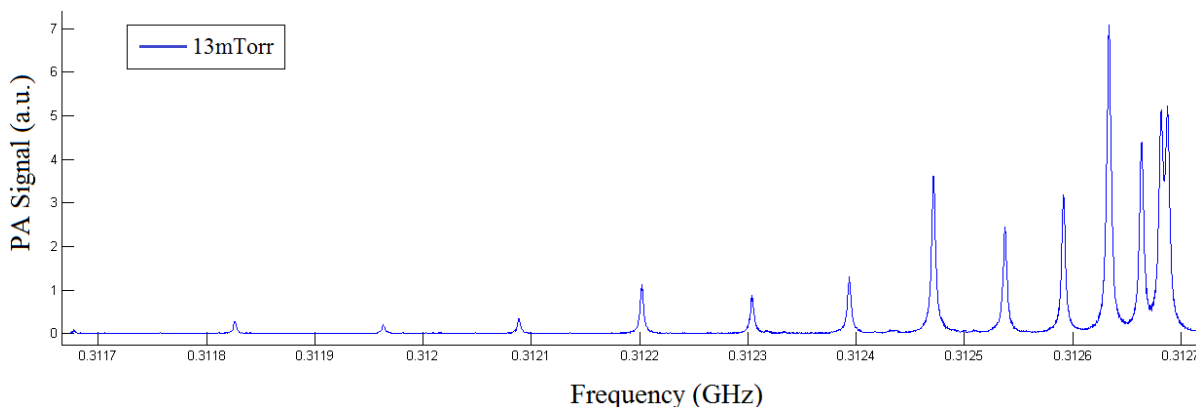
Figure 15. Methyl Cyanide absorption Lines taken at 13 mTorr from $0.3117 - 0.3127$ THz. This narrow spectrum shows 14 absorption peaks.

This graph shows 14 different absorption lines taken at 13 mTorr within a relatively narrow THz spectrum, from $0.3117 - 0.3127$ THz, a 1GHz band. This figure illustrates how methyl cyanide has very distinct absorption lines across a spectrum that we are interested in scanning, in this case, a 1 GHz band within the 0.3 THz region.

A THz source is also highly desirable due to its high tenability, low ionization energy, directionality, and material penetrating properties [3,60]. To generate the THz radiation and cause the photoacoustic effect, a Virginia Diodes Inc. (VDI) Amplifier Multiplier Chain 317 was used. The signal to the VDI THz radiation diode was provided by an Agilent E8254A PSG-A signal generator. The signal generator created an amplitude modulated square wave at the desired frequency and modulation pulse frequency which was configured through a LabView interface. Emitted power by the

THz VDI source ranged from 0.6 – 1.4 mW and is frequency dependent. On the opposite side of the chamber from the THz source, there's a VDI sensor positioned to measure the amount of power that exits the chamber. For this experiment, the amplifier chain used generated radiation over the 0.250-0.375 THz frequency range.

3.2 Test Chamber Design

A custom designed photoacoustic chamber was machined out of stainless steel to house the sensing element of the research project. This chamber is also where the gaseous sample is held and where the photoacoustic waves are generated. Figure 16 shows half of the photoacoustic cell.
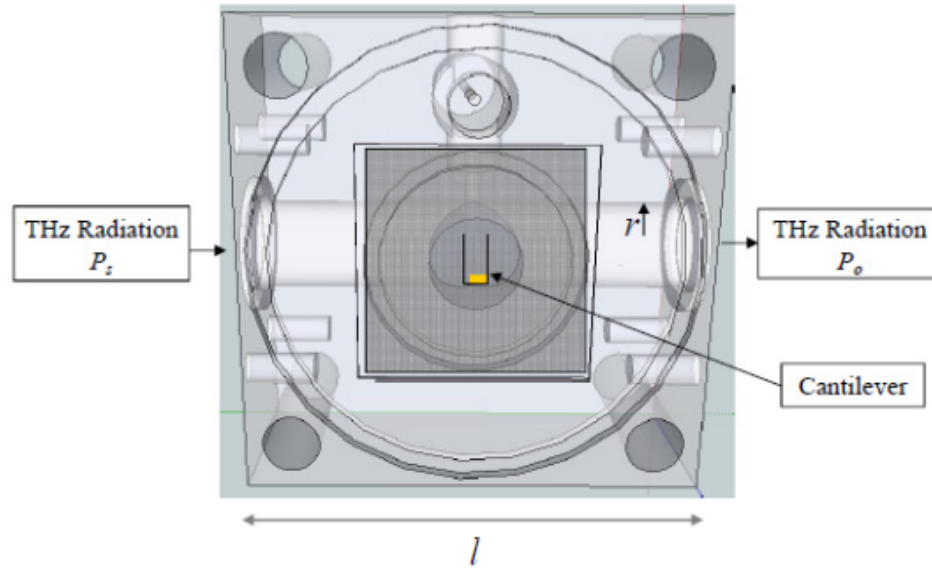
Figure 16. Schematic of back of photoacoustic test chamber [25]. Test chamber is 2x2x2 in^3 and machined from stainless steel. The absorption cell has a radius r = 0.197 in and is sealed at either end with Teflon windows. The cantilever sits between the two halves of the cell and is measured optically with a laser through a window in the front half of the cell.

The stainless steel cell is a cube with length l = 2 in and where the radius r = 0.197 in. The chamber consists of a front and back half and a 1 in^2 silicon sample, which acts as a

31

handle for the cantilever microphone, sits between the two pieces. The back half of the

chamber houses the absorption cell while the front half houses a balancing volume. In

order to maintain a seal on our gaseous sample, Teflon windows are used to seal the ends

of the absorption cells and an antireflective (AR) coated glass window seals the balance

volume which allows for the interferometer to make optical measurements of the

cantilever deflection. Figure 17 shows a photo of the test chamber.
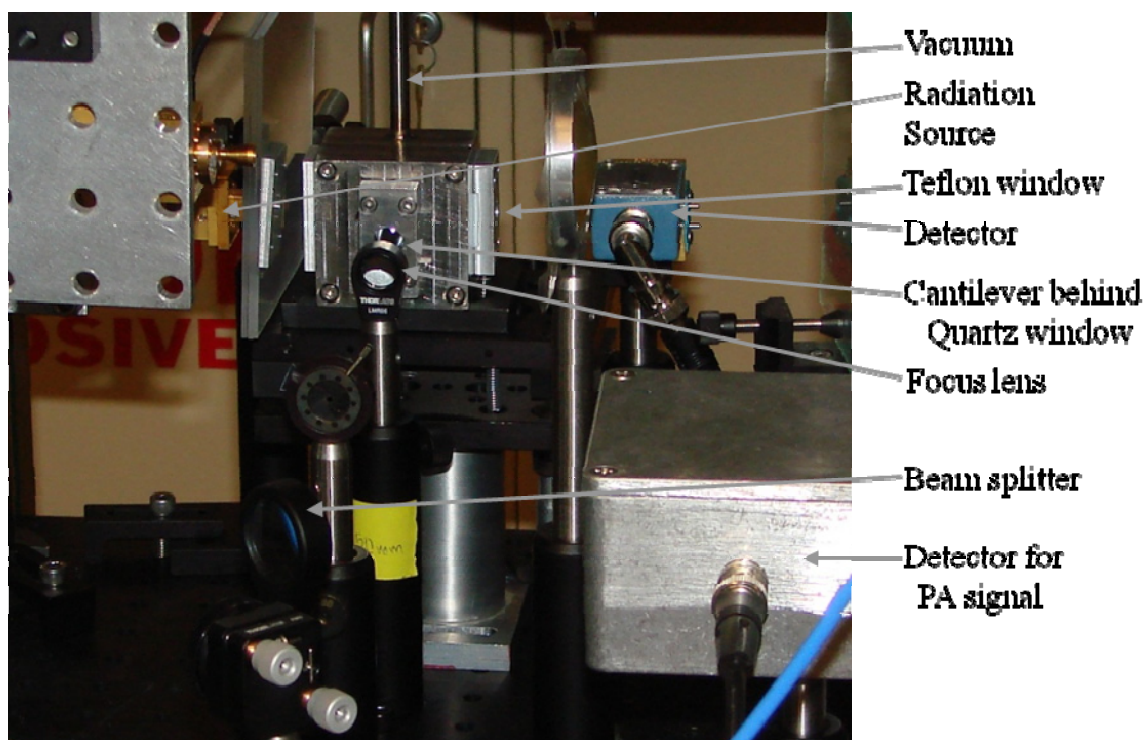
Figure 17. Photoacoustic test chamber shown along with vacuum tube, radiation source, Teflon windows, radiation detector, focal lens, beam splitter, and detector for photoacoustic signal [25].

A Pfeiffer HiCube™ turbo pumping station is used to evacuate the photoacoustic cell and

to achieve a low pressure, approximately 0.5 mTorr. Liquid CH_3CN is exposed to this

low pressure, which then vaporizes. The vapor is then slowly and carefully allowed into

the absorption chamber through a series of valves. This allows for a high degree of controllability in allowing discrete volumes of gas into our photoacoustic cell.

Measurements in the test fixture are made optically with a Michelson-type laser interferometer. A Helium (He)- Neon (Ne) laser beam is guided through a series of mirrors, beam splitters, irises, and focusing lenses and reflected off the Ti-Au spot on the tip of the cantilever. This reflected beam travels back to a photodiode where the laser beam power is measured. The irises serve to clip the beam, which lowers power as the beam sways due to cantilever deflection. By blocking a reference mirror in the test fixture, PA spectral data is collected. In order to quantify sinusoidal changes in power observed at the photodiode, the reference mirror is unblocked, which provides interferometric measurements. With these measurements, tip deflection measurements may be made through the generated interferometric signal. Figure 18 (not to scale) shows both the PA optical measurements by beam clipping when the reference mirror is blocked, and the Michelson interferometer displacement measurements when reference mirror is unblocked.
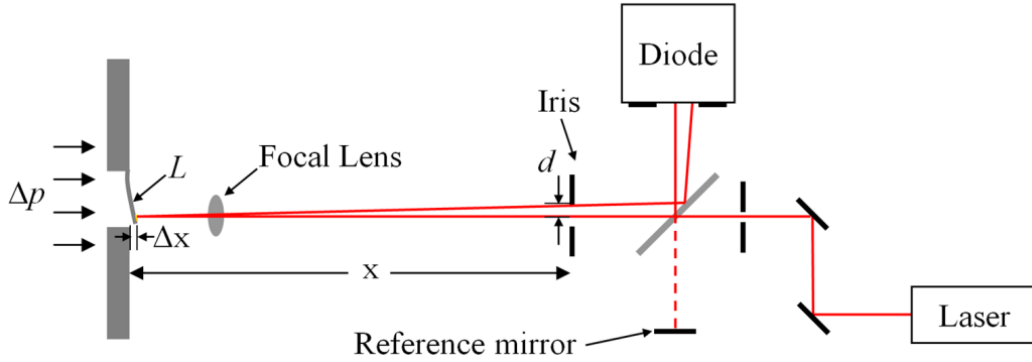
Figure 18. Diagram of laser measurements in test fixture [25]. As the laser is shifted due to the cantilever bending, part of the beam is clipped by an iris. This results in a loss of power at the diode. This changing power is measured and is how photoacoustic data is collected.

In both cases, the signal passes a Stanford Research Systems SR560 preamplifier that acts as a bandpass filter. The signal is also sent to a Stanford Research Systems SR530 lock-in amplifier. The modulated frequency from the Agilent signal generator is used as the reference in the SR530 lock-in amplifier.

3.2.1 Testing

Testing is done through the use of a Virginia Diodes Inc. THz radiation source that emits THz radiation through a Teflon window into the absorption volume in the test chamber. This volume sits "below" the cantilever and houses our gas species, methyl cyanide. This THz radiation is what causes the gas to heat and expand, inducing the PA effect. A THz source is chosen due to having fast modulation frequency as well as being able to pass through materials easily, such as the Teflon windows used to ensure a vacuum in the test chamber. Methyl Cyanide also has very strong absorption lines in the THz regime, which makes it a good candidate as a radiation source.

3.3 Modeling

By reviewing equations (4), (5), (6), and (7), it can be seen that maximum tip deflection results from increasing length (L) and decreasing width (w) and thickness (h). However, careful consideration must be taken into fragility of devices. Larger length to thickness ratios will lead to difficult to fabricate devices due to the fragile nature of high length to thickness ratio structures.

Initial cantilever designs were evaluated through the use of CoventorWare® FEM software. Using a harmonic modal analysis tool, a harmonic pressure load was applied to the cantilever surface as a function of frequency and the magnitude of the tip displacement was recorded. An important consideration in FEM modeling is the number of elements used to model the structure. Figure 19 shows a simulated cantilever with a 50x50x10 μm^3 mesh.
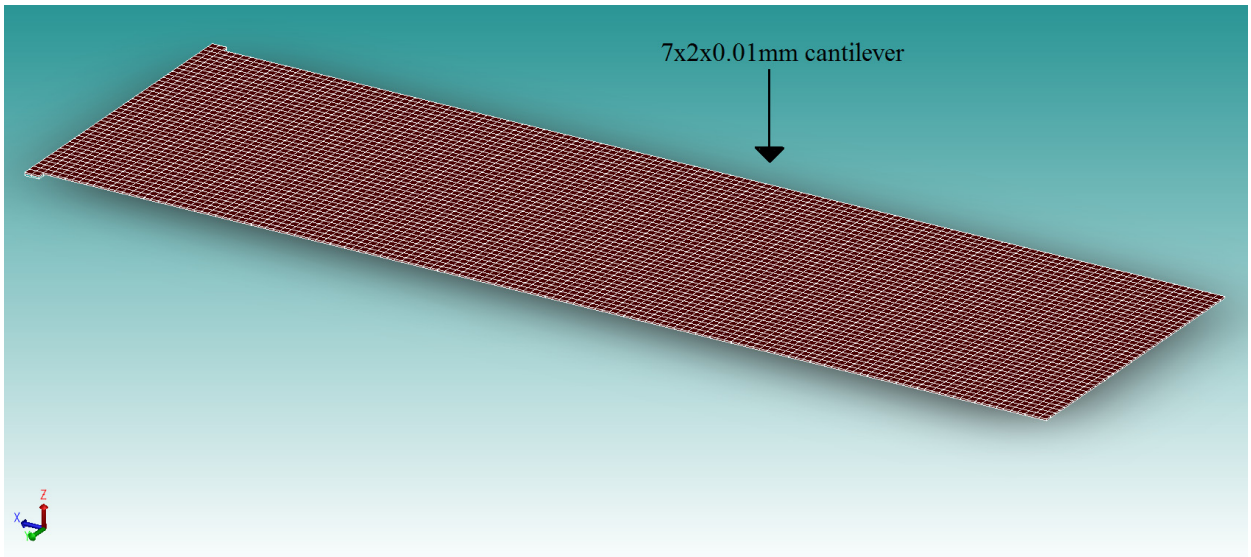
Figure 19. 7x2x0.01 mm³ cantilever with 50x50x10 μm^3 element simulated with CoventorWare® finite element methods (FEM) software.

A 50x50x10 μm^3 element is the largest element size used in modeling this cantilever, but still results in 5,600 finite elements in the mesh across the entire length of the beam. Each element must be simulated for during the entire frequency spectrum and through the modal harmonics, which results in a large number of computations. The finest mesh of 10x10x10 μm^3 blocks yields in 140,000 elements.

To increase the number of elements allows for more accurate simulations, but is very computationally demanding. This increase in computing time is nonconductive to running many simulations and a diminishing returns effect can be seen. As such, a mesh analysis was performed to find a suitable minimum elemental mesh size to obtain accurate results. Figure 20 shows a mesh analysis performed on CoventorWare[®] for a simulated 7x2x0.01 mm^3 cantilever.
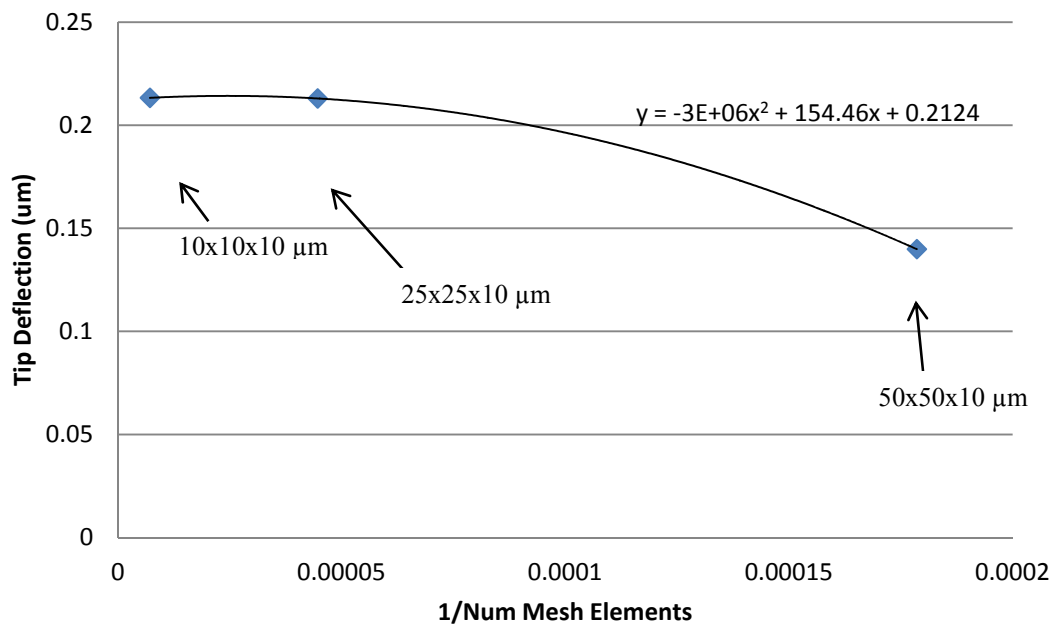
Figure 20. Mesh analysis showing that as the number of elements in a simulation approaches infinity, the deflection of a 7x2x0.01 mm^3 cantilever under a 0.1 mPa load approaches 0.214 μm. This analysis also shows that increasing the size of an element from 10x10x10 μm^3 to 25x25x10 μm^3 will more than halve computation time while only resulting in an error of 0.48% from the true value.

This mesh analysis shows a cantilever beam under a 0.01 mPA pressure load applied along the surface. This mesh study indicates that as the number of mesh elements approaches infinity, in other words, 1/number of mesh elements approaches 0, the tip deflection should approach a value of 0.214 μm. This study is important in justifying larger meshes, which yields fewer elements which reduces computation times. An increase in mesh dimensions from 10x10x10 μm^3 to 25x25x10 μm^3 reduces run times by over 50% but only yields in a difference in results of 0.26% and an error from the estimated true value of 0.48%. With a suitable sized mesh, a proper series of simulations may be run to simulated cantilever bending, resonant frequency, modal harmonics, and various other cantilever aspects. Figure 21 shows a completed CoventorWare$^®$ simulation with the first modal harmonic being displayed.
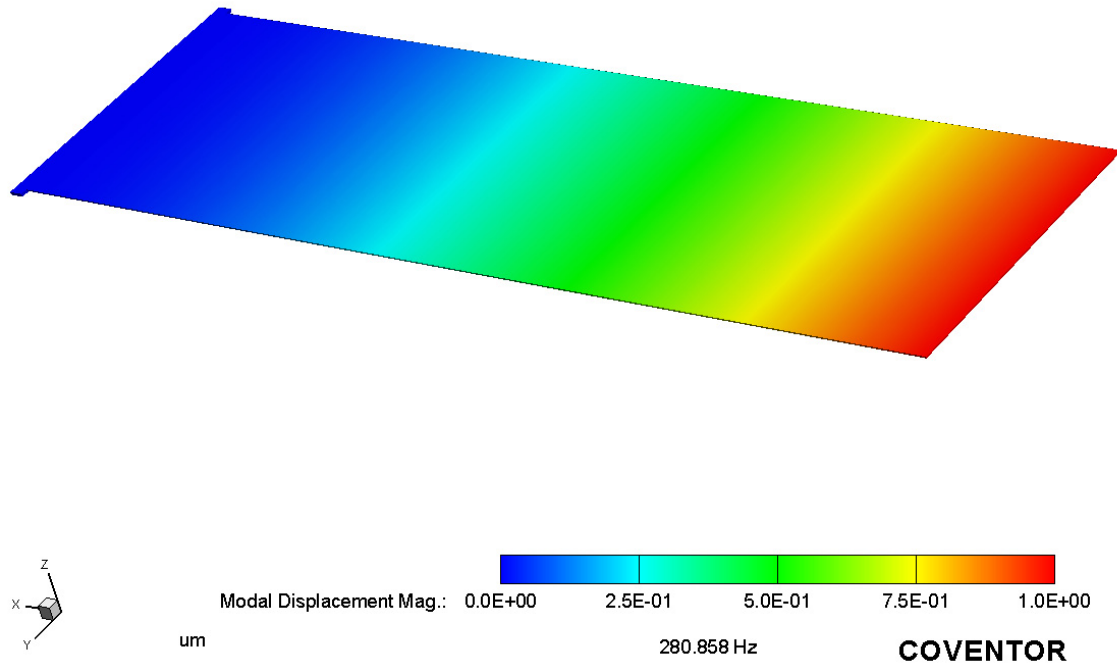
Figure 21. CoventorWare® simulation of 7x2x0.01 mm³ cantilever at first modal harmonic at 280.858 Hz.

This simulation shows the first modal harmonic of the cantilever appearing at 280.858 Hz.

3.4 Cantilever Fabrication

The fabrication process is done on an n-type SOI wafer. First, a thin layer (200/1000 Å) of titanium/Gold (Ti/Au) is evaporated onto the tip of the cantilever as a reflective surface for the interferometer. The titanium acts as an adhesion layer for the gold, which does not normally stick very well to silicon. Next, the device layer is patterned, with photoresist and spun to a thickness of ~2 μm and exposed in an MJB3 mask aligner with the proper device layer mask. It is exposed with UV light for ~8 s and receives a power dosage of approximately 150 mJ/cm² in order to pattern the resist which

is then developed and baked. Next, the sample is etched using DRIE to create a gap between the device layer from the surrounding membrane. This gap distance must be tightly controlled for if it is too large, it allows for gas leakage between the cantilever and surrounding membrane. This membrane gap and associated gas leakage controls the damping of the system. Too much leakage and the system becomes undamped and no longer functions properly since undamped systems will only oscillate at the structure's resonant frequency. Figure 22 shows a schematic of the device layer gap along with an optical image of the gap.
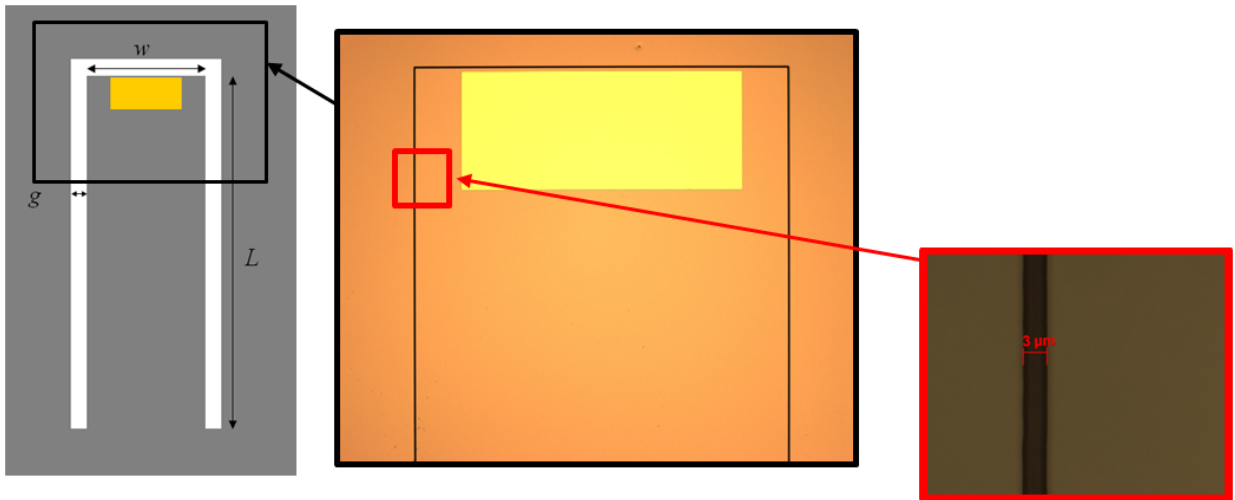
Figure 22. Device layer gap along the edge of the cantilever beam separates the cantilever from the surrounding membrane [25]. This gap is important in controlling the damping of the cantilever system. Too large and the cantilever becomes undamped, which results in the cantilever only vibrating at resonant frequency.

Through experimentation and modeling, it is found that a 3 μm gap is smallest membrane gap achievable through DRIE. It is possible to form the gap through RIE, but the resulting gaps were found to be ~8 μm.

After the topside DRIE, the back of the sample must undergo DRIE to reach the oxide layer. This oxide is subsequently etched away with HF vapor, releasing the device.

However, the layer of oxide between the device layer and substrate leads to residual stress in the membrane directly behind the base of the cantilever, causing the beams at rest to bend upwards. This is due to the residual stress $\Delta\sigma$ in the cantilever, which, using Equation (7), can be calculated. Using R = 1.11 m, the resting radius of curvature of a fabricated cantilever, Eγ = 169 GPa, which is the Young's Modulus for silicon, ν = 0.064 which is the Poisson's ratio corresponding to the crystal orientation of the bending cantilever and d = 10 μm, which is the thickness of the beam, it is shown that the cantilevers have an internal stress gradient $\Delta\sigma$ = 2.702 N/m [26].

To counter this bending, a layer of oxide was thermally grown at the top of the device layer. As an oxide is grown on the surface of silicon, this caused the phosphorous atoms that our n-type wafer was doped with to gather at the surface [8]. In other words, the growing oxide drives phosphorous atoms towards the oxide. The larger phosphorous atoms accumulating towards the top of the device layer results in residual stress bending the cantilever back into plane, which is shown in Figure 23. Figure 24 shows the fabrication steps from a cross sectional view of the sample.
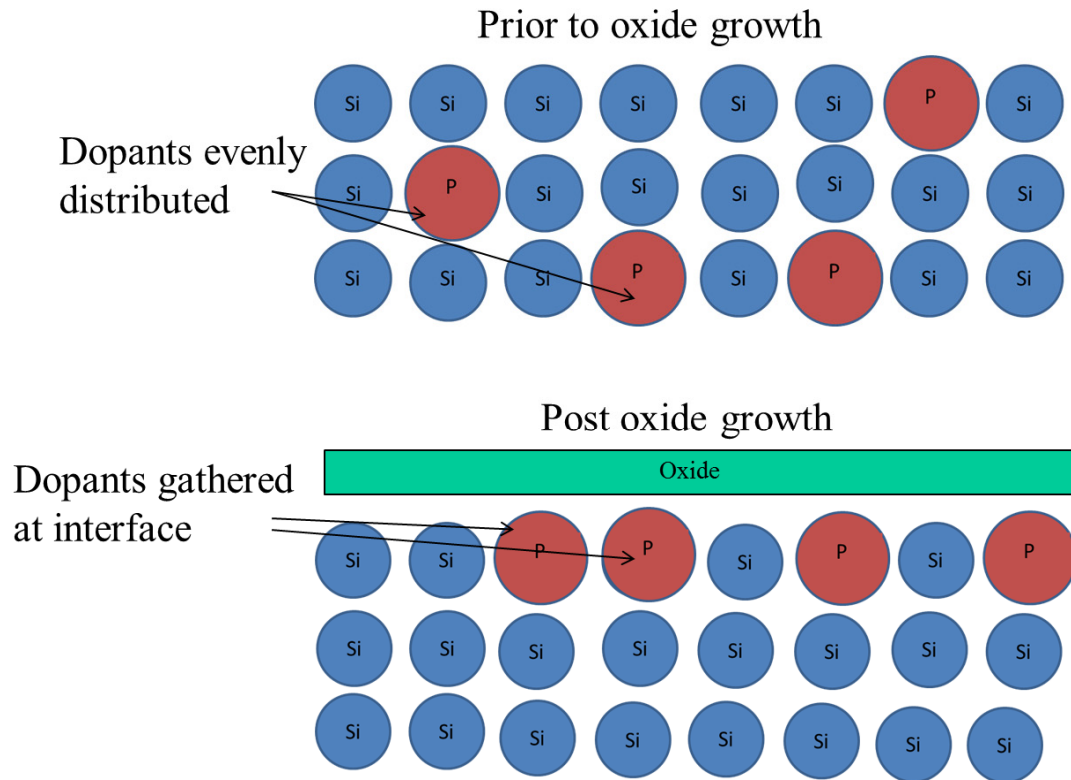
Figure 23. Diagram of effect of oxide growth on n-type silicon doped with phosphorous atoms. Prior to oxidation, phosphorous atoms are spread evenly through silicon. After oxide growth, phosphorous gathers at the interface, which causes the silicon to stress away from oxide growth due to the phosphorous atoms being larger than surrounding silicon atoms.
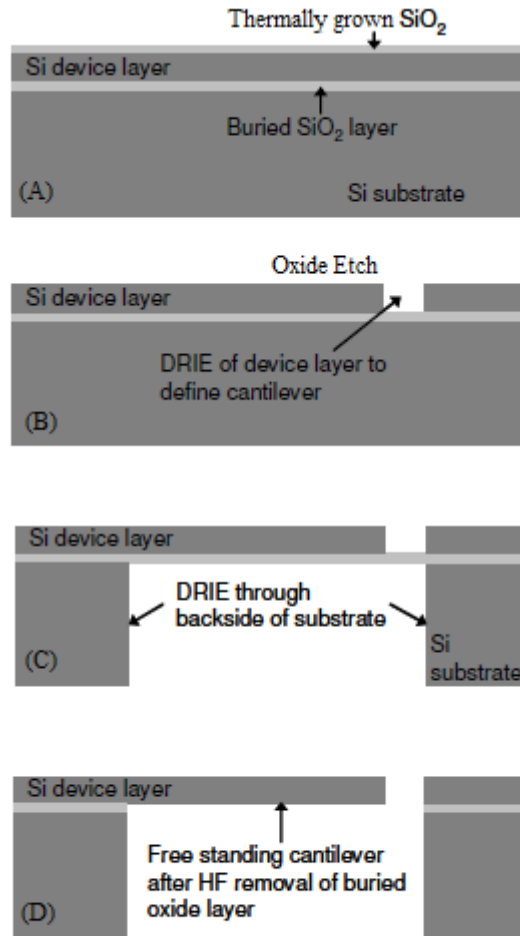
Figure 24. Fabrication steps for improved cantilever fabrication process. First, an oxide is grown in an oxidation furnace at 1000º C. Then the oxide is etched away, the cantilever is shaped with deep reactive ion etching (DRIE). The backside of the handle wafer is also etched to the buried oxide and finally the oxide is removed through a hydrofluoric vapor etch.

After release, cantilever curvature is measured using a NewView™ Zygo white light interferometer. This interferometer works by reflecting light onto a surface and then using the resulting fringe lines documented on the surface to measure surface topography. These fringe lines result from the white light emanating varying wavelengths which reflect off a surface. As these waves bounce back, some constructively interfere while

42

others destructively interfere. It is this interference that causes the fringe lines which are then evaluated through software to perform accurate measurements.

Another source for loss of sensitivity in previously fabricated cantilever systems is the rounded corners shown in Figure 11. This is due to the etch profiles of wet etchants traditionally used to release cantilevers having an isotropic etch profile. This research effort includes the use of a HF vapor etch. This HF vapor etch allows for a higher degree of selectivity between the oxide layer and the mechanical, silicon layer. The HF vapor etches at approximately 0.3 µm / min and results in significantly tighter corners along the edge of the cantilever beam. The etch continues until it is optical verified that all oxide has been removed from the bottom of the cantilever. Due to the thin nature of the oxide diffracting light, it is very noticeable when oxide remains on the surface. Figure 25 shows an optical image of oxide that has not been completely removed during device release.
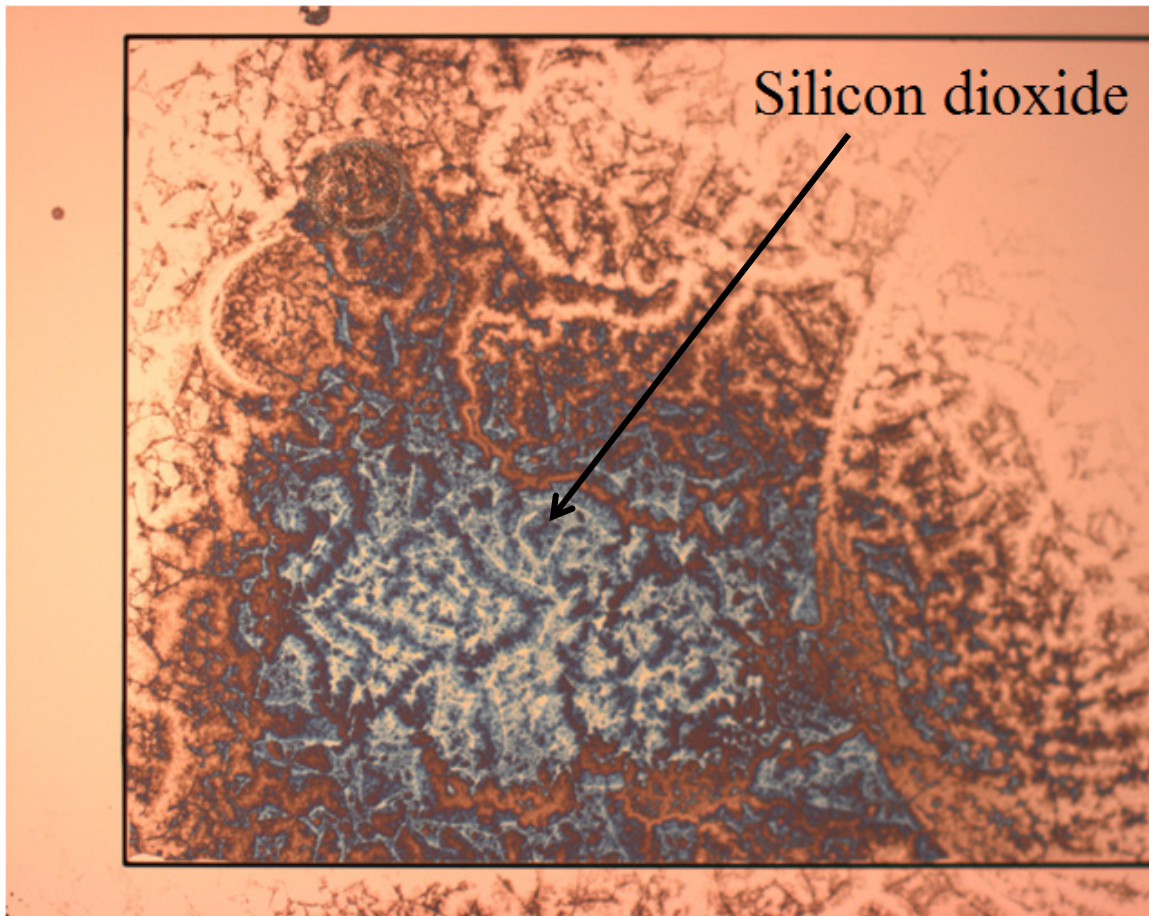
Figure 25. Oxide on the bottom of a cantilever remaining after release. This remaining oxide will cause the cantilever beam to curl by as much as 100 μm if not completely etched away.

 Once all the oxide has been etched, the cantilever is fully released and ideally maintains

a small gap around the entire length of the cantilever beam. Figure 26 shows an optical

image of a corner of the cantilever beam.
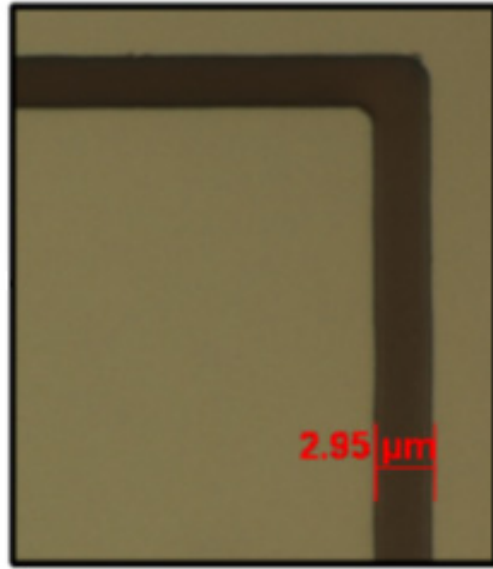
Figure 26. Corner of cantilever beam showing the tight ~3 µm gap that exists along the entire length of the beam, including the corner [25].

As can be seen, the membrane gap is maintained throughout the entirety of the beam, which limits gas leakage, which increases sensitivity in the cantilever devices. This process of dry etching also provides less force upon the cantilever during the release process than would be applied during submerging and surfacing of the sample into a liquid etchant. With high length to thickness ratios (700) careful consideration must be taken into handling of the cantilever during and after release. It is due to this high fragility that the longer 7 mm cantilevers are only fabricated on 10 µm SOI, since the 5µm devices yield such a low percentage of working devices and are prone to snapping and cracking along the cantilever / membrane gap. Figure 27 shows a cantilever where the small 3µm gap had been over-etched to become much larger and a close-up on the top right corner where a hairline fracture had developed in the membrane.
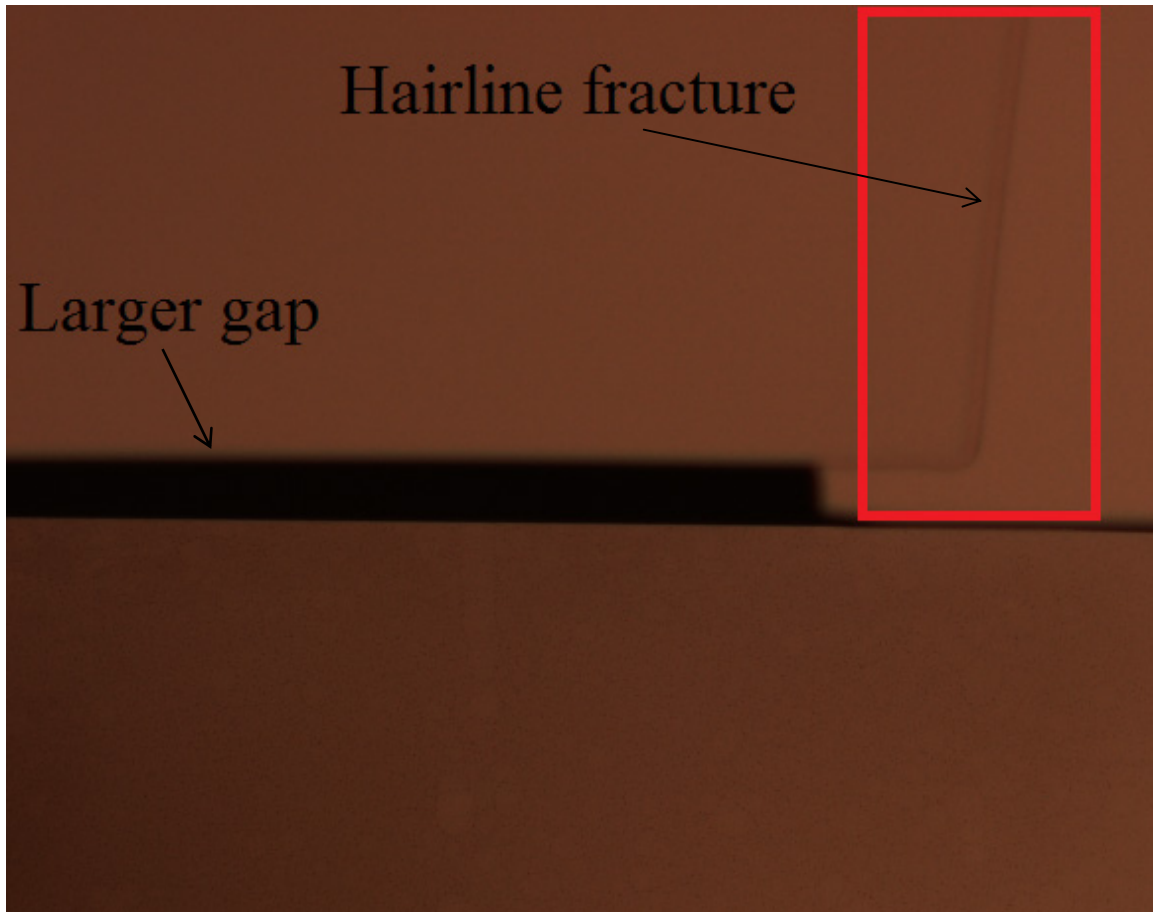
Figure 27. Cantilever with large gap and cracked membrane. This large gap was due to over-etching during the release process and a hairline fracture that formed along the membrane.

However, once released the cantilevers are less prone to fracturing since they become separated from the membrane by the gap along the edge of the beam. The cantilever beams are relatively flexible and can bend with minor vibrations or impacts. It is during the release process that they are most fragile, but care must still be taken when handling released cantilevers.

Previous students have made several attempts at fabricating piezoelectric cantilevers using a PZT target to sputter PZT onto a cantilever. However, before another attempt was done by this research effort, an analysis of the PZT target was conducted. A

chemical composition done by electron dispersive spectroscopy (EDS) was performed on

the target and it was determined that the target was severely deficient in lead, which is

necessary for PZT to have adequate piezoelectric properties [22,30]. Figure 28 shows the

results of the EDS scan on the PZT target.
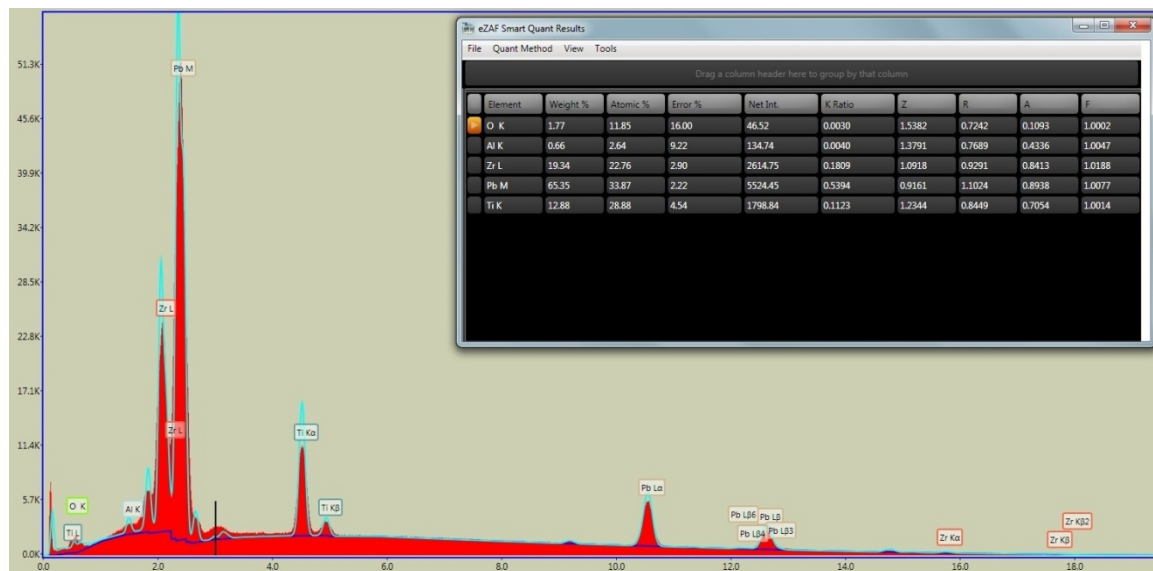
Figure 28. Electron dispersive spectroscopy (EDS) results performed on the lead zirconate titanate (PZT) target used in previous attempts at fabricating piezoelectric cantilever. It is shown that the target has a lead deficiency, which inhibits proper piezoelectric properties in material sputtered from this target.

The EDS result shows a PZT target with a lead concentration of 33%, which is smaller

than required for a good thin film of PZT to be sputtered and have piezo properties. With

this knowledge, any future attempts at fabricating PZT coated cantilever for this research

effort were no longer considered.

IV. Data

Chapter Overview

This chapter details the results of developing sensitivity improved cantilevers. The improvements to fabrication techniques are discussed as are the physical results of these modifications. The changes made to the cantilevers include: oxide growth prior to fabrication, modification to cantilever dimensions, and shaping the geometry of cantilevers. Each of these changes and their impacts on cantilever sensitivity are discussed.

4.1 Cantilever Geometry

As shown earlier in Figure 27, during release, the membrane surrounding the cantilever is prone to fracturing. This is due, in part, to the large surface area being only 10 μm thin making the silicon prone to cracking due to high length to thickness ratios. This is especially true of the area of silicon closest to the corner of the cantilever. The sharp right angle has a high stress concentration that makes the silicon prone to cracking due to accidental force or when the silicon is slightly weakened by the release process [27]. To counter this high stress concentration, the edge of the cantilever has been filleted in order to reduce the stress concentration and to improve survivability and yield of cantilevers. Figure 29 shows the filleted corner of a cantilever.

Figure 29. Filleted corner of cantilever is used to reduce stress in the membrane caused at the sharp right angle that previously existed. The tight ~3 µm gap is still maintained throughout the corner.

This rounded corner has reduced the number of cracked membranes of fabricated cantilevers by roughly 50%. The number of cracked membranes is very nearly tied to yield of cantilevers since the cantilevers are relatively robust prior to being released and the membrane is the most likely to fracture during release.

4.2 Cantilever dimensions

Cantilever sensitivity is also a function of cantilever dimensions, which affects resonant frequency and deflection. Ideally, an incredibly long, narrow, and thin cantilever would produce the most sensitive device. Unfortunately, fragility comes into play when

dealing with such devices. While prior students and other research efforts have had success with 5x5x0.005 mm³ devices, these devices have been difficult to fabricate and handle due to their extremely fragile nature. This research effort focused on thicker, 10μm cantilevers but increased the length to 7 mm in order to compensate for lost sensitivity. Figure 30 shows the expected results from an increase in cantilever length.
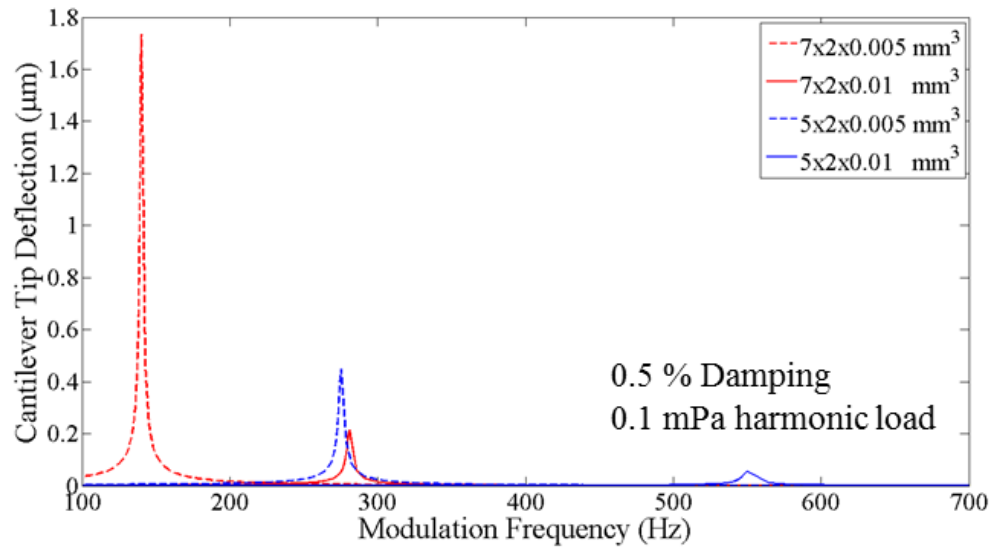
Figure 30. CoventorWare® simulation showing effect of increasing cantilever length [25]. In both the 5 μm thick beams and 10 μm thick beams, increasing the length from 5 mm to 7 mm results in an increased cantilever tip deflection by up to 4x.

However, while longer cantilever dimensions provide more deflection, increasing length also decreases the delta in between the first two modal harmonics of the cantilever.
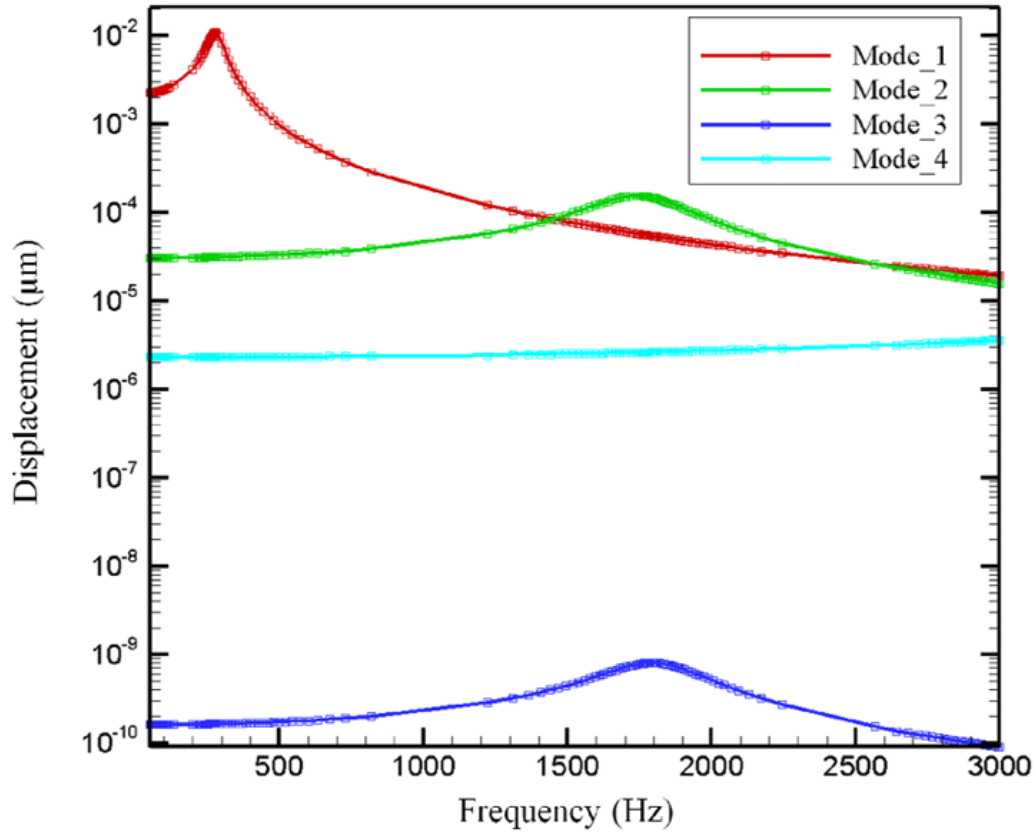
Figure 31. CoventorWare® simulation showing first four modal harmonics of a simulated 7x2x0.01 mm³ cantilever and the amount of tip deflection that occurs at these frequencies [25]. It is primarily the first two modes that contribute to tip deflection.

As the length of a cantilever continues to increase, the delta in between the first two modes will decrease, until it becomes difficult to vibrate a cantilever at resonant frequency without unintentionally exciting higher vibrational modes. However, this effect is limited at a length of 7 mm, which still leaves a delta of ~1500 Hz. For a review of the first two modal harmonics of a variety of cantilever dimensions, reference Appendix E.

4.3 Thermal Oxidation

Previously fabricated cantilever beams did not yield perfectly flat cantilevers. As a result, sensitivity loss was incurred due to the beam's resting position leaving a larger

51

than 3μm gap around the beam. This large gap is a source of gas leakage. Figure 32 shows the measurements of a previously fabricated cantilever.
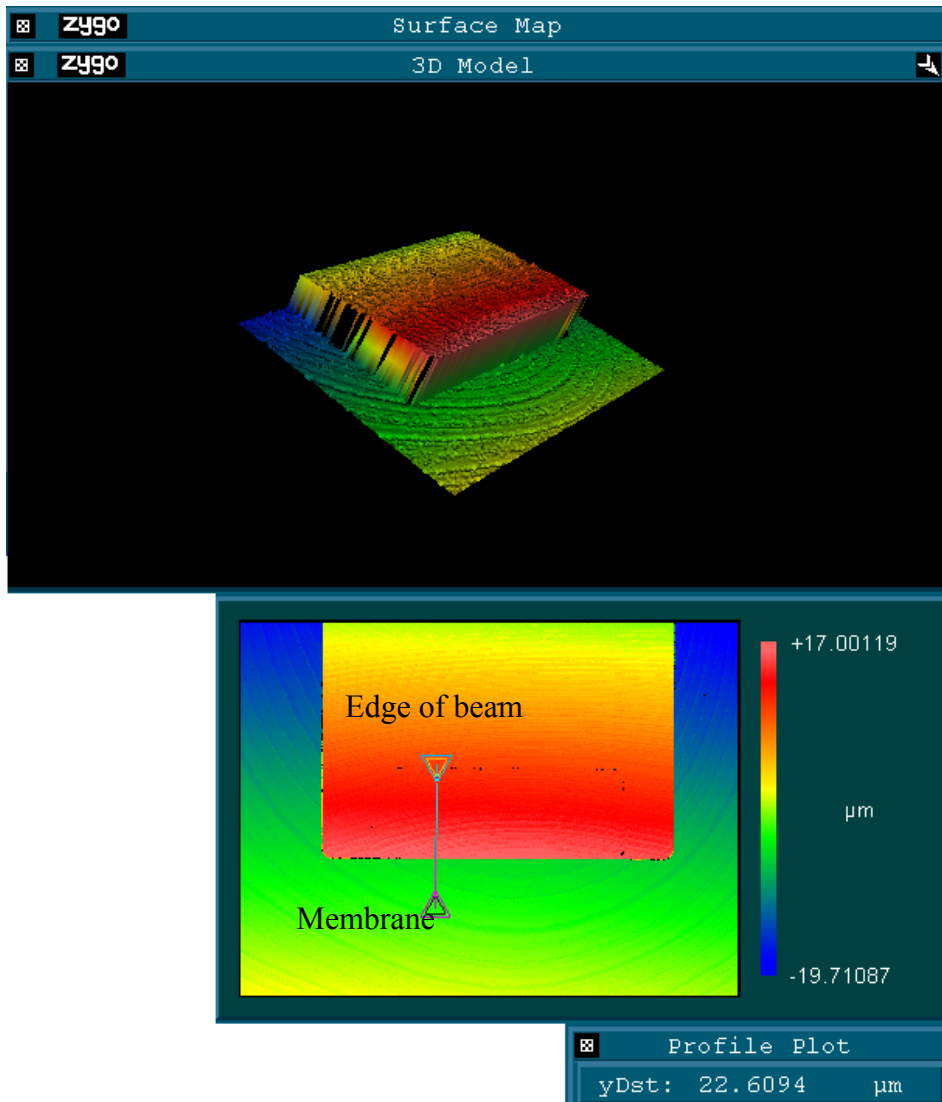
Figure 32 (a). Surface map of cantilever as shown by Zygo^{TM} white light interferometer. The resting curvature of this cantilever beam is 22.6 μm out of plane measured from the tip to the membrane directly across from it.

Figure 32(a) shows a 3D model of the surface of the cantilever (top) based on the optical image formed with white light interferometer image (bottom) along with the out of plane curvature as measured by the interferometer.
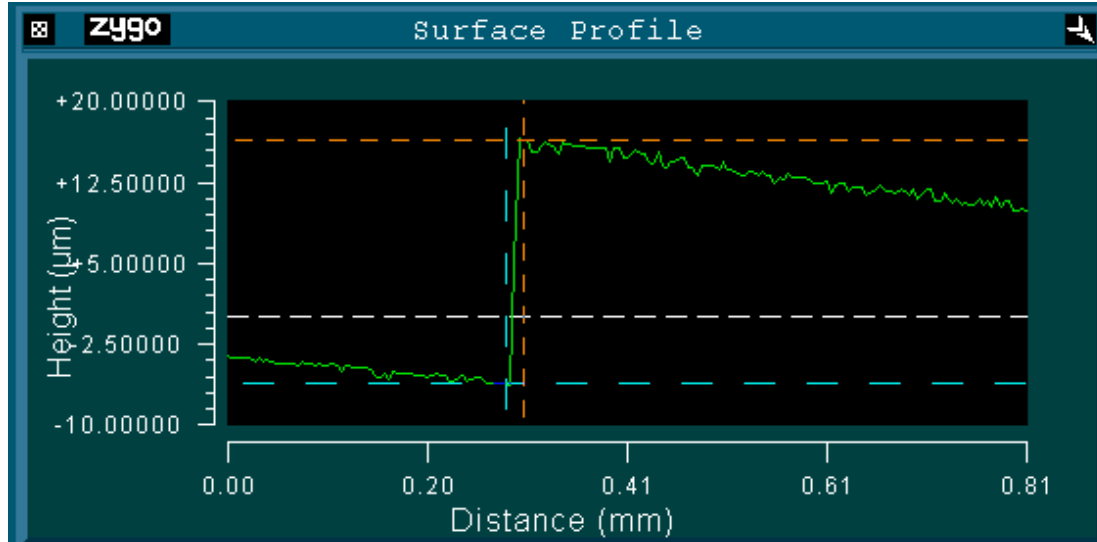
Figure 32 (b). Zygo[TM] white light interferometer measurement of cantilever showing the graph of displacement of the top of the cantilever along the length of the beam.

Figure 32 (b) shows a graph of displacement in the x-direction along the length of the cantilever.

Prior to device fabrication, a layer of thermal oxide is grown on top of the SOI. This allows the silicon to be converted into SiO_2 at a rate of 44% Si per unit SiO_2. This conversion also changes the beam geometry, but due to the relatively small amount of oxide grown relative to the device layer thickness (0.1 μm compared to 10 μm) this effect is negligible. This causes the phosphorous atoms in the n-type Si to gather at the oxidation site. The phosphorous atoms gathering along the interface causes the remaining Si to tend to stress towards the handle. This is due to phosphorous atoms being larger than the surrounding silicon atoms. Oxides were grown in a wet thermal oxidation furnace at 1000º C for 1,2,3, and 4 hours. The resulting oxide thicknesses are recorded in Figure 33.
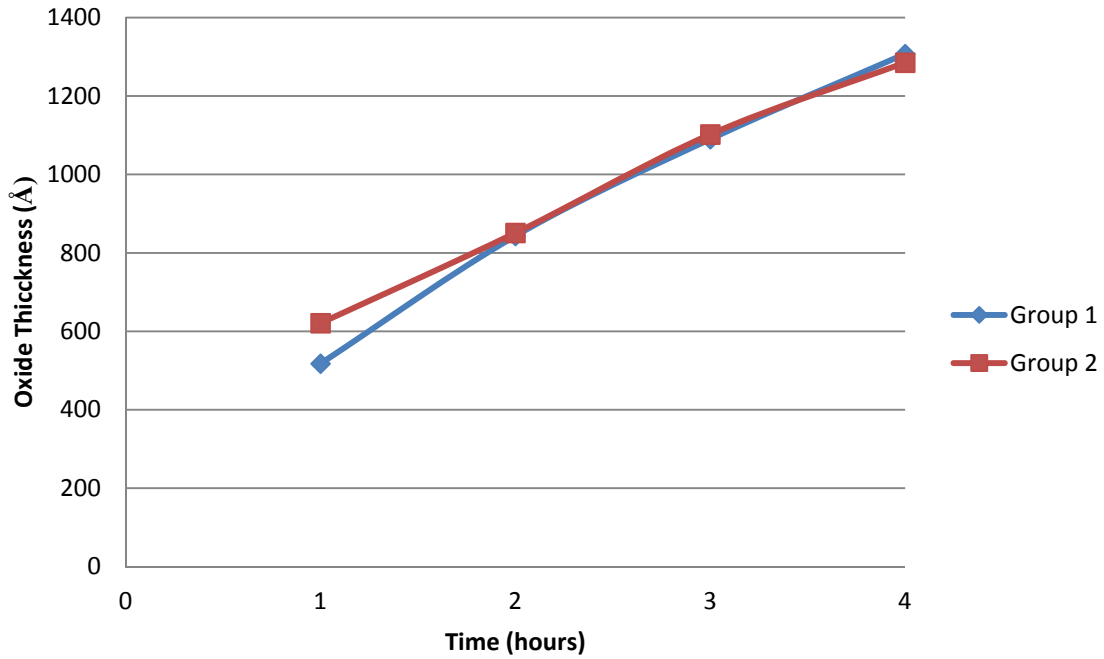
Figure 33. Plot of oxide thicknesses over time of two sets of samples. The samples were put into an oxidation furnace at 1000º C for 1,2,3, and 4 hours.

As seen in Figure 33, the oxide thicknesses tend to grow linearly as a function of time in the furnace. The oxide thicknesses are measured via a Zygo^{TM} white light interferometer.

After cantilever release, the resting deflection out of plane is then measured with the Zygo^{TM}. The measurements are shown in Figure 34.
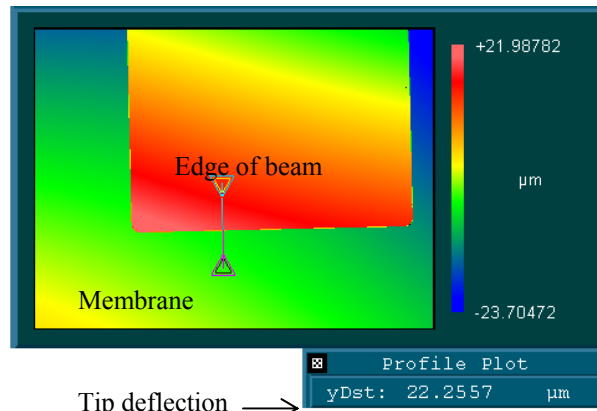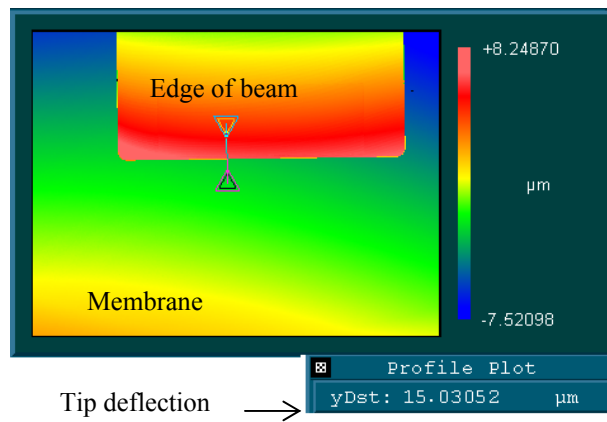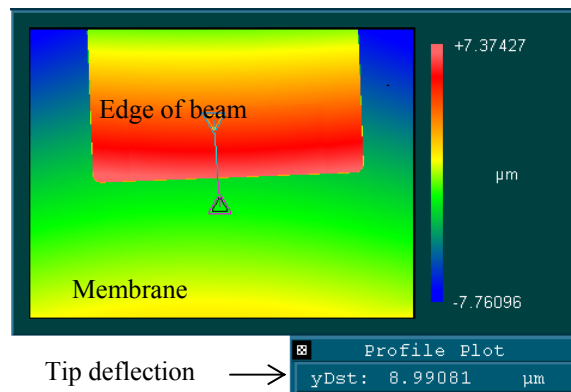
Figure 34. Cantilever deflections out of plane for 1 (a), 2 (b), and 3 (c) hours. As can be seen, the more oxide grown on the surface of the beam prior to fabrication, the less the resulting tip deflection

The resulting radii of curvature are then plotted against oxide thickness. Unfortunately, both 4 hour oxide growth samples did not make it to device release. One was mishandled, causing it to shatter, and the other had SU-8 photoresist sputtered into the DRIE etch hole when the DRIE carrier wafer lost thermal contact with the samples.
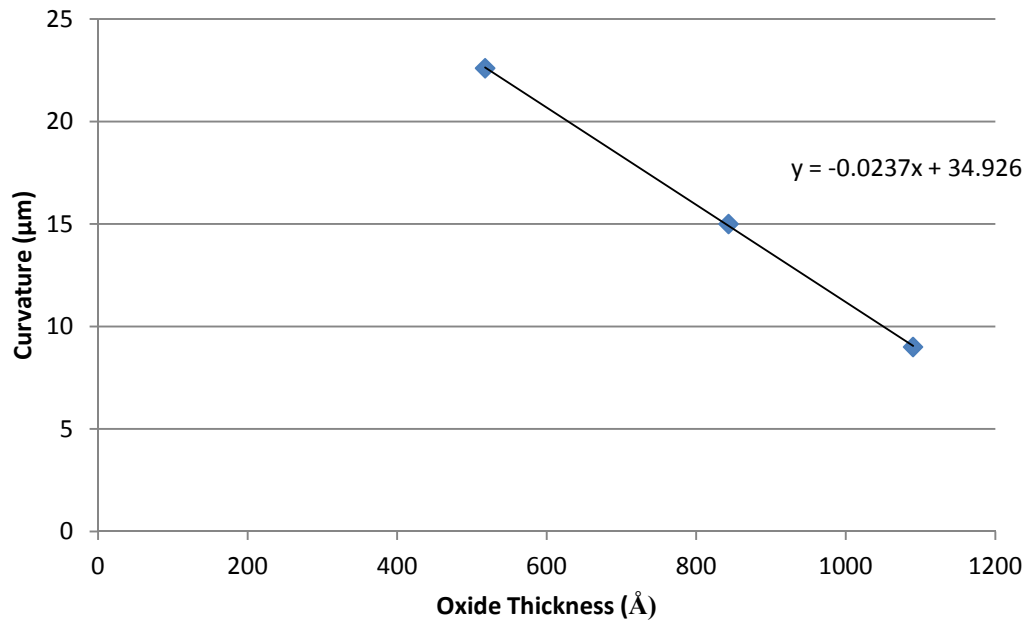
Figure 35. Plot of cantilever curvatures vs oxide thickness. The curvatures decrease linearly with amount of oxide grown prior to fabrication. Only 3 points are shown due to the 4 hour samples shattering prior to device release.

As can be seen, as the oxide grown becomes thicker, the curvature out of plane of the device becomes smaller, indicating a flatter resting state which allows for less gas leakage during sensing. This is due to the reasons discussed earlier, to include the diffusion of phosphorous atoms into the silicon and the annealing effects of the furnace required to grow the oxide. As gas leakage around the tip of the cantilever is reduced, the spring constant of the systems increases as more gas stays behind the device to allow for more effective damping. This increase in damping allows for more sensitive gas sensing.

56

While no four hour sample survived, it can be predicted that the resulting curvature out of plane would have been roughly 3.96 μm. This can be inferred due to the linear nature of the graph of curvature to oxide thickness.

4.4 Spectral Data

All other things being equal, a flatter cantilever should result in a more sensitive device due to the cantilever deflecting more in both directions. Next, spectral data is collected to measure and compare the relative sensitivities of the flatter cantilever that is the result of this research effort with prior results. Figure 36 displays methyl cyanide spectra collected at 15 mTorr.
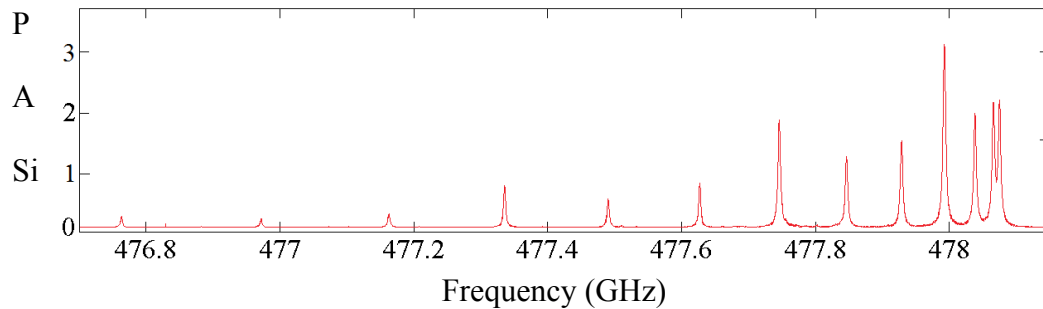
Figure 36. Methyl cyanide spectra of 7x2x0.01 mm cantilever beam taken at 15 mTorr along a ~1.5 GHz spectrum. The collection shows strong absorption lines as well as high signal to noise (SNR) ratios.

Upon first inspection, the spectra looks clean with strong absorption lines and comes close to matching the performance of the previously fabricated 5μm device.
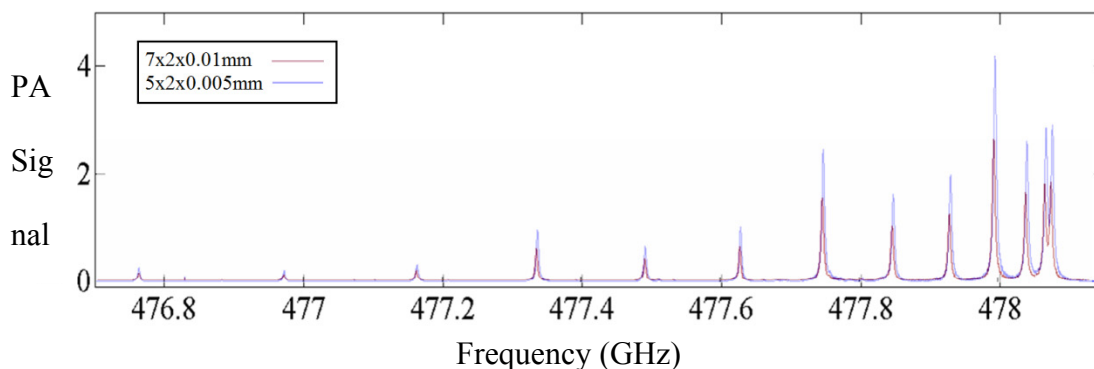
Figure 37. Overlay of methyl cyanide spectra of 7x2x0.01 mm^3 design and 5x2x0.005 mm^3 design. The 7 mm design does not have as high a response as the 5 mm design, but that is expected due to the 7 mm design being twice as thick. However, the peaks match very closely.

As seen in Figure 37, the two spectra collections line up very closely. However, as can be expected, the 5μm device still outperforms its longer, thicker counterpart. This spectra utilized a 0.2 MHz step size with an excitation of 4s, followed by a signal averaging time of 0.5 s. This data collection took 9.1 hours to perform, during which the chamber pressure rose by 5 mTorr. This spectra was collected with a cantilever that had oxide grown for 3 hours in the furnace. The long data collections are due to the cantilever requiring a long excitation time due to slow response times at lower pressures. Figure 38 shows the varying results from varying the excitation time. This spectrum was collected by previously fabricated 5x2x0.010 mm^3 cantilever.
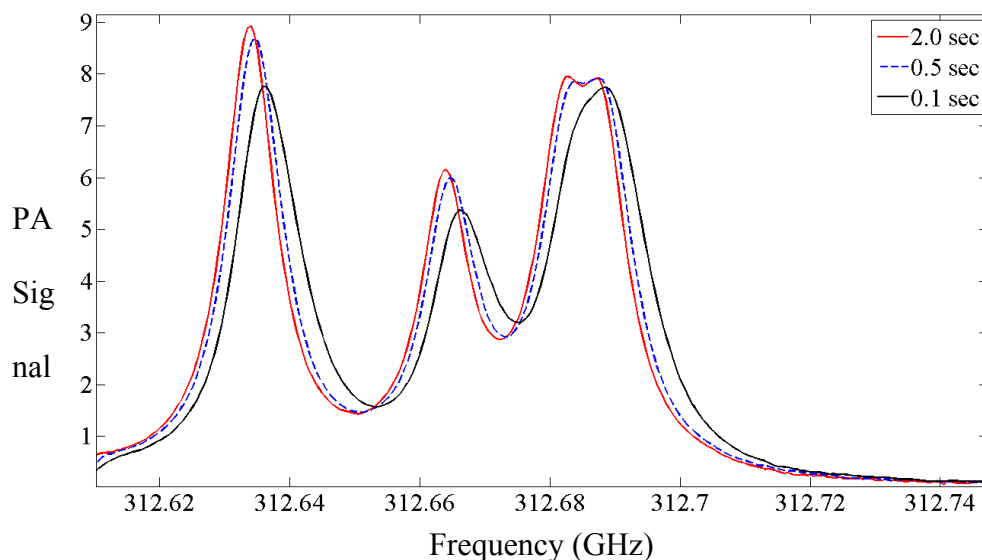
Figure 38. Spectra PA signals taken at 38 mTorr with varying excitation times [25].

As can be seen, lowering excitation time both increases the peak response to higher frequencies and lowers the amplitudes of the PA signal. This is due to the low excitation pressure generated in the chamber due to the low overall pressure. Under low pressures, the excitation time for a single data point collect can be roughly 4-12 s. In order to best collect data, the cantilever should be at steady state prior to data collection. However, due to the large sizes of spectrums that are being scanned and the small step sizes, waiting too long for the cantilever to reach steady state can unnecessarily increase data collection times. In order to illustrate the time it takes to reach steady state, the amplitude of the PA signal is graphed against time as shown in Figure 39 and Figure 40.
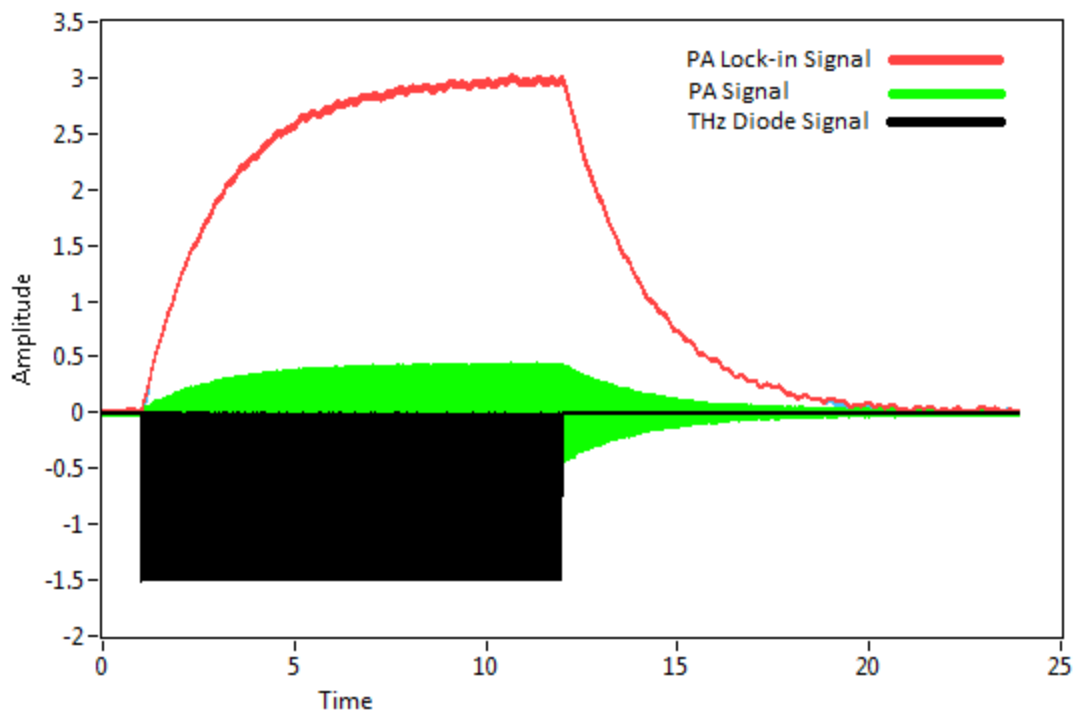
Figure 39. Photoacoustic (PA) data recorded at 11 mTorr. At this pressure, the PA signal continues to grow until about 8 s, after which the cantilever reaches steady state.

As displayed, the PA signal from the cantilever continues to grow until roughly 8 seconds, after which the cantilever reaches steady state. After the THz radiation is turned off, the exponential decay of the PA signal can also be seen. This also contributes to the time taken in between data collects in order to ensure the cantilever has come to rest prior to being re-excited. This slow decay is also due to the small damping coefficient and continued excitation at a lower absorption strength, causes the amplitude deflection to reduce slowly. These times become drastically reduced at higher pressures as shown in Figure 40.
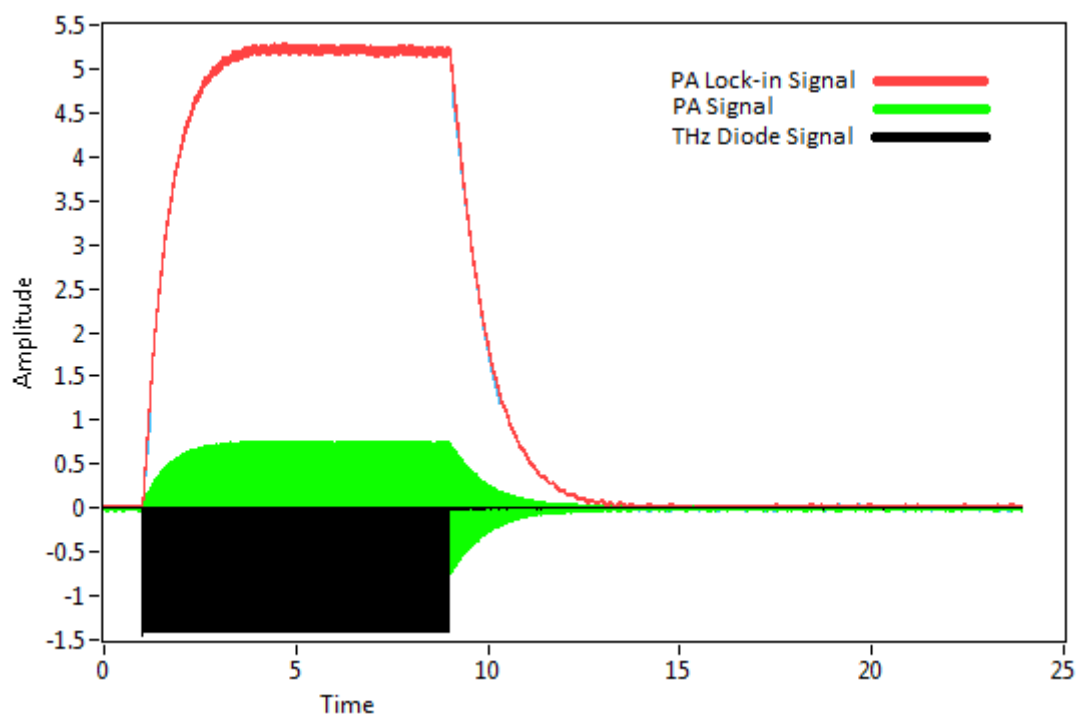
Figure 40. Photoacoustic (PA) data recorded at 78 mTorr. At this pressure, the PA signal reaches steady state much quicker than previously recorded at 11 mTorr.

By increasing the pressure from 11 mTorr to 78 mTorr, the excitation time required drops

from 8 s to 3 s. These times required are compared to chamber pressure in Figure 41.
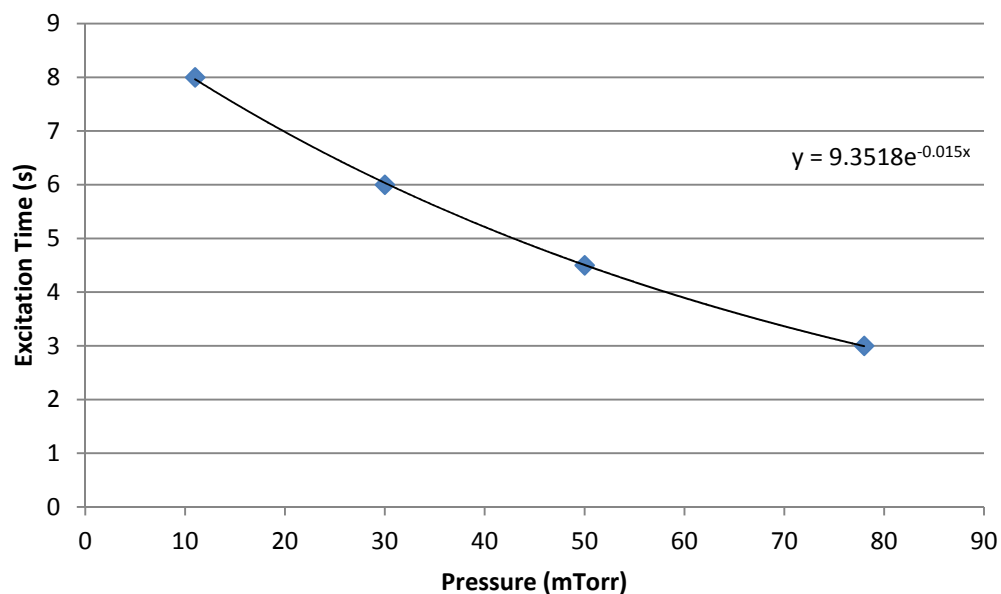
Figure 41. Plot of excitation time required vs chamber pressure. It can be seen that as pressure increases in the chamber, the amount of time required to bring the cantilever to maximum deflection decreases.

However, by increasing pressure, the resolution and sensitivity of our systems decreases

as shown in Figure 42.
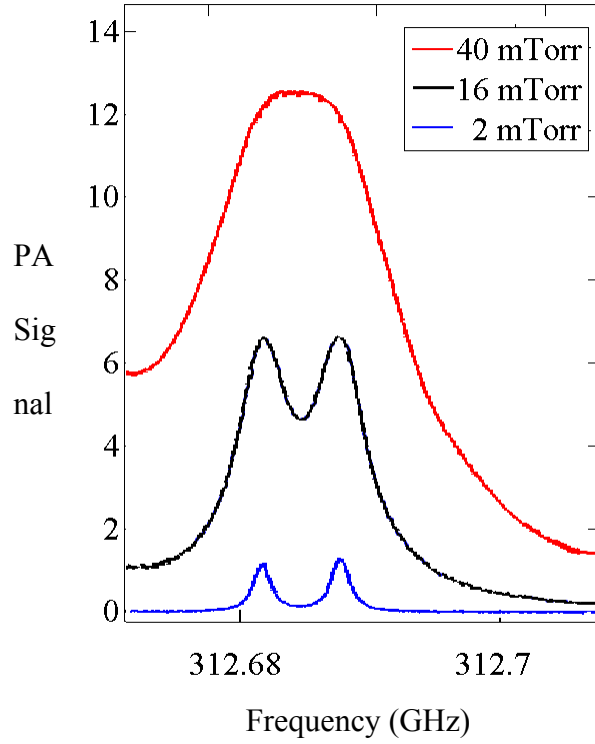
Figure 42. PA spectra collected at varying chamber pressures. As the pressure increases in the chamber, the resolution of the system decreases. At 40 mTorr, two absorption peaks that are apparent at 2 mTorr become indistinguishable.

As can be seen, with a higher pressure, the last two absorption peaks begin to blur into one large peak as the pressure raises from 16 mTorr to 40 mTorr. This resolution is quantified as the quality factor of the cantilever. Quality factor (Q) can be expressed as

$$Q = \frac{\omega_0}{\Delta\omega} = \frac{f_0}{\Delta f} \qquad (9)$$

where f_0 is the resonant frequency of the cantilever and Δf is the full width half max of the PA signal. Figure 43 shows how quality factor of a system changes with chamber pressure.
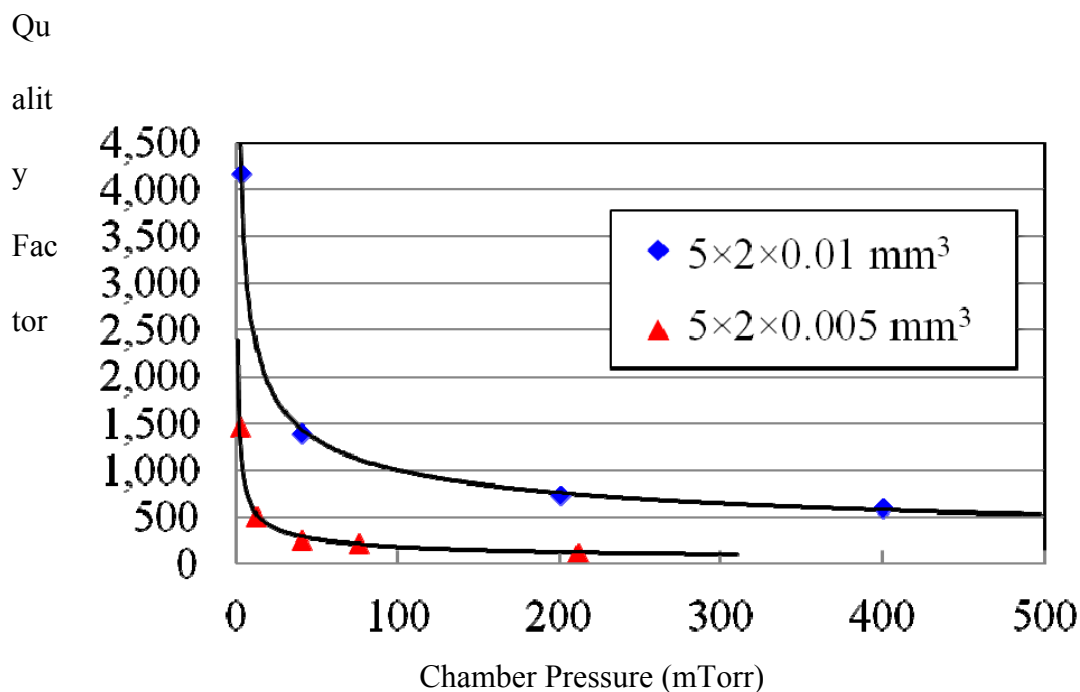
Figure 43. Quality factors, based on Equation (9), of cantilevers previously fabricated with dimensions of 5x2x0.01 mm³ and 5x2x0.005 mm³ [25]. This plot shows how quality factor decreases sharply with increase of chamber pressure.

While an increase in chamber pressure may decrease the response time for a cantilever to reach steady state, it will suffer in terms of specificity. A system with a low quality factor may incapable of distinguishing one gas species from another. To keep high quality factors, chamber pressure must be kept low, and photoacoustic collections will take longer.

While these long data collects seem impractical, they are unnecessary for basic chemical identification. A fast scan technique with a low excitation time at a higher chamber pressure could be used to quickly evaluate small spectral regions for absorption lines in order to give a quick identification of an unknown chemical. Lower chamber pressures and long excitation times can then be used to identify line center absorption frequencies and the relative PA amplitudes for each absorption line.

<div align="center">

V. Analysis

</div>

Using the PA spectra collected, the performance of the system is evaluated and compared against prior research. The SNR is determined by finding the maximum and minimum signals found in the spectra. The noise level of the PA measurement must be measured away from strong rotational absorption lines and away from any weak excited state vibrational absorption lines. To locate the noise floor, the root-mean-squared (RMS) value of the signal was calculated by

$$Signal_{RMS} = \sqrt{\frac{(s_1{}^2 + s_2{}^2 + \cdots + s_n{}^2)}{n}} \qquad (\,10\,)$$

Where n is the number of samples in the interval and s is the PA signal value measured at each frequency step. A sample size n = 100 consecutive samples provides a conservative RMS noise floor for the PA spectral data, and is used for the remainder of the analysis. The calculated SNRs are shown in Table 1 for various data collections.

Table 1. SNR results for multiple sample size intervals

Sample Size	Max Signal	RMS Noise	SNR
10	3.0127	0.0009	3,347.4
25	3.0127	0.0015	2,008.5
50	3.0127	0.0017	1,772.2
100	3.0127	0.0019	1,585.6
200	3.0127	0.0025	1,205.1
500	3.0127	0.0028	1,076.0

The SNR of the system varies across the collections due to several reasons. Settings on the photodiode and lock-in amplifiers required adjustment for large versus small cantilever deflections since large deflections causes PA signals greater than 10V, which

would overload the DAQ card's ±10 V limit. Spectrums were also collected over large frequency ranges which required longer times which allowed more time for external noise to be introduced into the system. This noise in the PA system and in the measurements are discussed in a later section.

Next, the sensitivity of the device is evaluated. Using the equation for α_{min} , the sensitivity of the device can be calculated based on the absorption strength and the SNR corresponding to the measurement. The best sensitivity was found to be 1.71×10^{-5} cm^{-1}.

Table 2. Best sensitivity results for cantilever designs compared to prior research.

Cantilever Design (mm^3)	Chamber Pressure (mTorr)	Radiation Frequency (GHz)	α_{peak} (cm^{-1})	SNR	α_{min} (cm^{-1})
5x2x0.01	13	312.633	0.02400	1,221	1.97×10^{-5}
7x2x0.01	13	312.633	0.03450	2,012	1.71×10^{-5}
5x2x0.005	38	459.627	0.05387	3,719	1.13×10^{-5}

As can be seen in Table 2, the sensitivity of this device improves upon previously fabricated 10μm devices. However, many factors have changed between prior students and the current search effort, to include chamber design, laser, the THz source has been changed, and the chamber mount has been adjusted and also may have made the system more susceptible to vibrational noise.

To help account for some of these variations, the NNEA , which takes into account the radiation source output power and the sampling time, is calculated. The results are shown below in Table 3.

Table 3. Best NNEAs achieved by the system compared to prior results.

Cantilever Design (mm^3)	Chamber Pressure (mTorr)	P_0 (µW)	T(s)	NNEA (cm^{-1} W $Hz^{-1/2}$)
5x2x0.01	13	~100	0.5	1.39×10^{-9}
7x2x0.01	13	~25	1	4.28×10^{-10}
5x2x0.005	38	~25	1	2.83×10^{-10}

As can be seen, the sensitivity-improved cantilever improved the NNEA of the 10µm cantilever-based system by 69% while only being outperformed by the 5µm cantilever by 33%.

There are two factors used in the sensitivity and NNEA calculations which have some margin of error associated with then. The first potential source of error is the peak absorption coefficient (α_{peak}) extracted from the simulation software which was used to calculate the sensitivity. The other factor that was estimated to as close a degree as possible was the power output of the THz radiation source. There are insertion losses in power as the radiation entered the PA chamber, depending how close the source was to the Teflon window. Fluctuations in the THz diode output power are frequency dependent, which also contributes to the uncertainty of the power used to calculate the NNEA.

VI. Conclusions

Chemical sensing and PA spectroscopy is an area of research with many possibilities for both commercial and military applications. Designing and fabricating the sensitivity improved MEMS cantilever sensors and analyzer was a multidisciplinary effort, which requires incorporation of chemistry, physics, and engineering principles. In this research effort, sensitive PA cantilever sensors were successfully designed, modeled, fabricated, and tested under very low chamber pressures for THz chemical spectroscopy. Design parameters of length, width, thickness, as well as an initial thermal oxidation growth of the cantilever structures were analyzed and compared and used to improve upon previous cantilever designs that were sensitive to the low pressures generated in the stainless steel PA test chamber. Along the path to creating these sensitive devices, several fabrication processes and techniques were improved upon to make this effort successful. The compact PA THz spectroscopy system developed in this work is significantly smaller than traditionally used long path gas phase molecular spectroscopy systems which presents the possibility of portable spectroscopy systems.

6.1. Fabrication

Several contributions to the previous work done at AFIT in designing, fabricating, and testing MEMS cantilever PA sensors were accomplished in this work. Through the improvement of previously established fabrication processes, very sensitive MEMS cantilever PA sensors were created. The inclusion of a thermal oxide growth to help alleviate internal stresses allow for a degree of control in the resting curvatures of cantilever beams. The best designed beam had a curvature of roughly 9μm out of plane,

68

and due to the 10μm thickness of the beam, this ensures that the 3μm gap between the beam and membrane is intact along the entire length of the beam. Survivability of the cantilevers were also improved upon by fileting the corners of the beam. This filet reduces residual stress in the membrane that tends to crack. While not as crucial on the more robust 10μm designs, this filet could greatly improve yield on potential 5μm designs.

6.2. Sensitivity Results

In this research effort, the custom fabricated THz photoacoustic spectroscopy system achieved a sensitivity of 1.71×10^{-5} cm^{-1} and a NNEA of 4.28×10^{-10}cm^{-1} W Hz$^{-1/2}$. While this did not achieve the same sensitivity of previously fabricated 5μm devices, it lays the groundwork on how to improve upon designs. By improving upon the 10μm design by as much as 69%, it is reasonable to assume that if the same changes to cantilever dimension were done on a 5μm device, that sensitivity results would continue to be improved.

6.3. Future Research

As well as fabricating a 7x2x0.005 mm^3 cantilever, recommendations for future work would include adding a piezoelectric layer onto the cantilever design. This would allow for a footprint reduction in a PA test setup. A piezoelectric sensor configuration would provide a compact way of evaluating the cantilever response to the PA pressures and the optical measurement method could be used in tandem with or potentially be eliminated entirely, depending on the piezoelectric performance. The cantilever fabrication process was developed to ensure the device layer surface was protected during

every step of the fabrication sequence. PZT or ZnO are promising piezoelectric layers that could be implemented into the designs. The protective photoresist layer used during the cantilever release process would completely protect the piezoelectric materials from the strong HF vapors.

Internal stresses in the cantilever are alleviated through thermal oxidation of the SOI prior to fabrication but may not be necessary through modifications to the selection of SOI. Reducing the buried oxide (BOX) layer thickness to ~0.2µm on the SOI wafer would greatly reduce the residual stress built up in the device layer and may remove the need for thermal oxidation, or require less of it to result in cantilever with no to little resting curvature. A 0.2 µm BOX would still be thick enough to serve as an effective etch stop for the DRIE step of the handle. Also, the final step in cantilever release involves removal of the BOX with HF vapor. Any inadequate coverage of the protective photoresist layer may result in etching and depositing films onto the device layer. A BOX layer of 0.2 µm would etch in 20% of the current etch time and may also reduce risk of damaging the cantilever surface.

The PA laser beam clipping measurement technique allowed for an accurate deflection measurement, which utilized low data sampling rates. However, Converting the experimental setup and data collection to a Michelson configuration would allow the optical layout to be further reduced in size by eliminating the beam clipping iris, making the system even more compact. Higher resolution can also be achieved if a data acquisition card with a higher sampling rate is acquired.

Appendix A. Visual Bibliography

A visual bibliography is a great tool to help sort through a literature review. It visually represents keywords common throughout literature pertinent to this research effort and links documents based upon these keywords. Seeing which papers share common keywords allows a user to easily sort through works and find those most relevant. Figure 44 shows such a visual bibliography where the numbers shown are reference numbers in the bibliography.
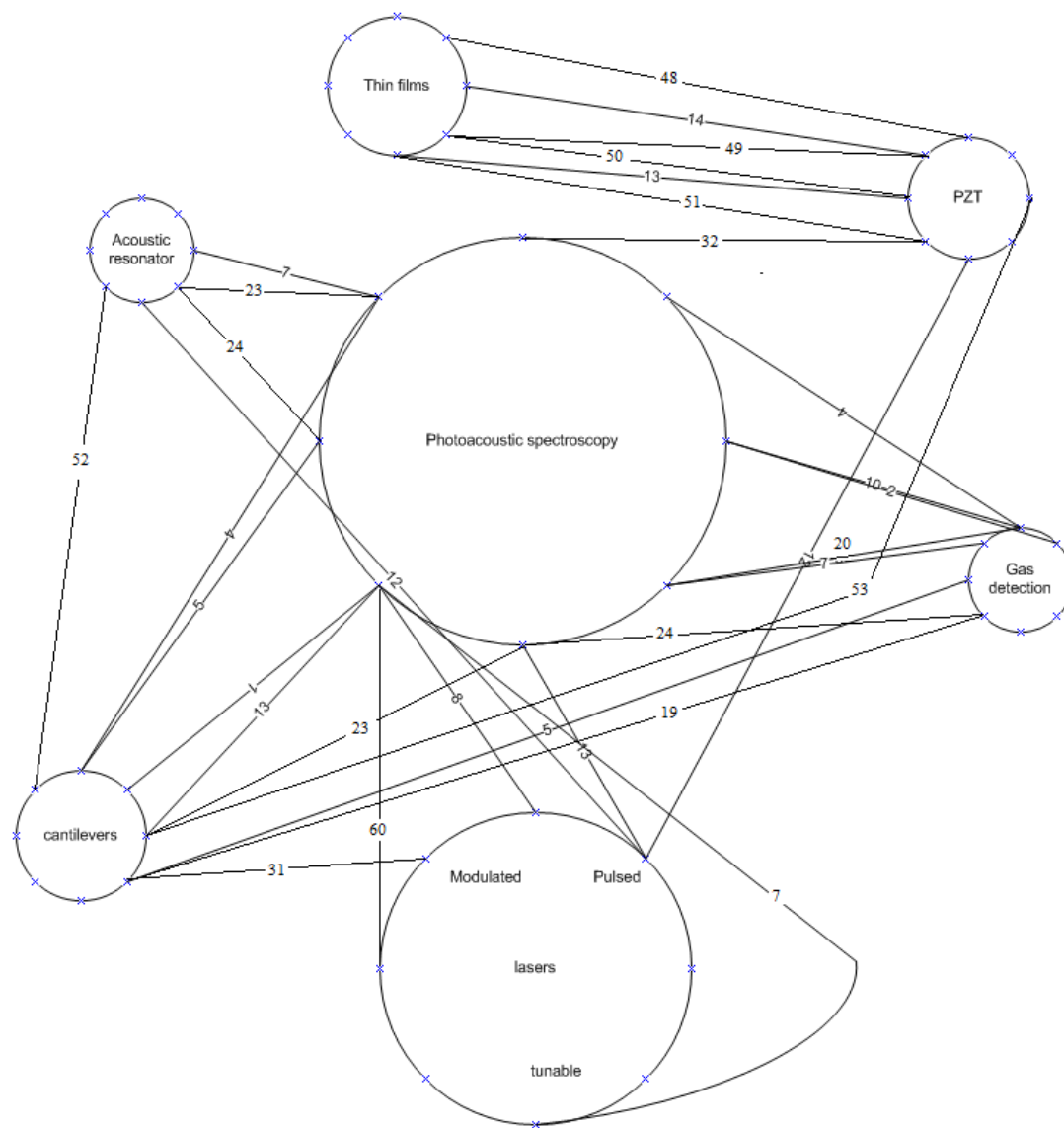
Figure 44: Visual bibliography relating keywords shown in the circles. The numbers along the connecting lines are the reference numbers of articles in the bibliography.

Appendix B. Mask Layouts

Shown below are the individual masks used for fabrication. These masks were designed through the use of L-Edit and written with a Heidelberg instruments µPG 101 lithography system.
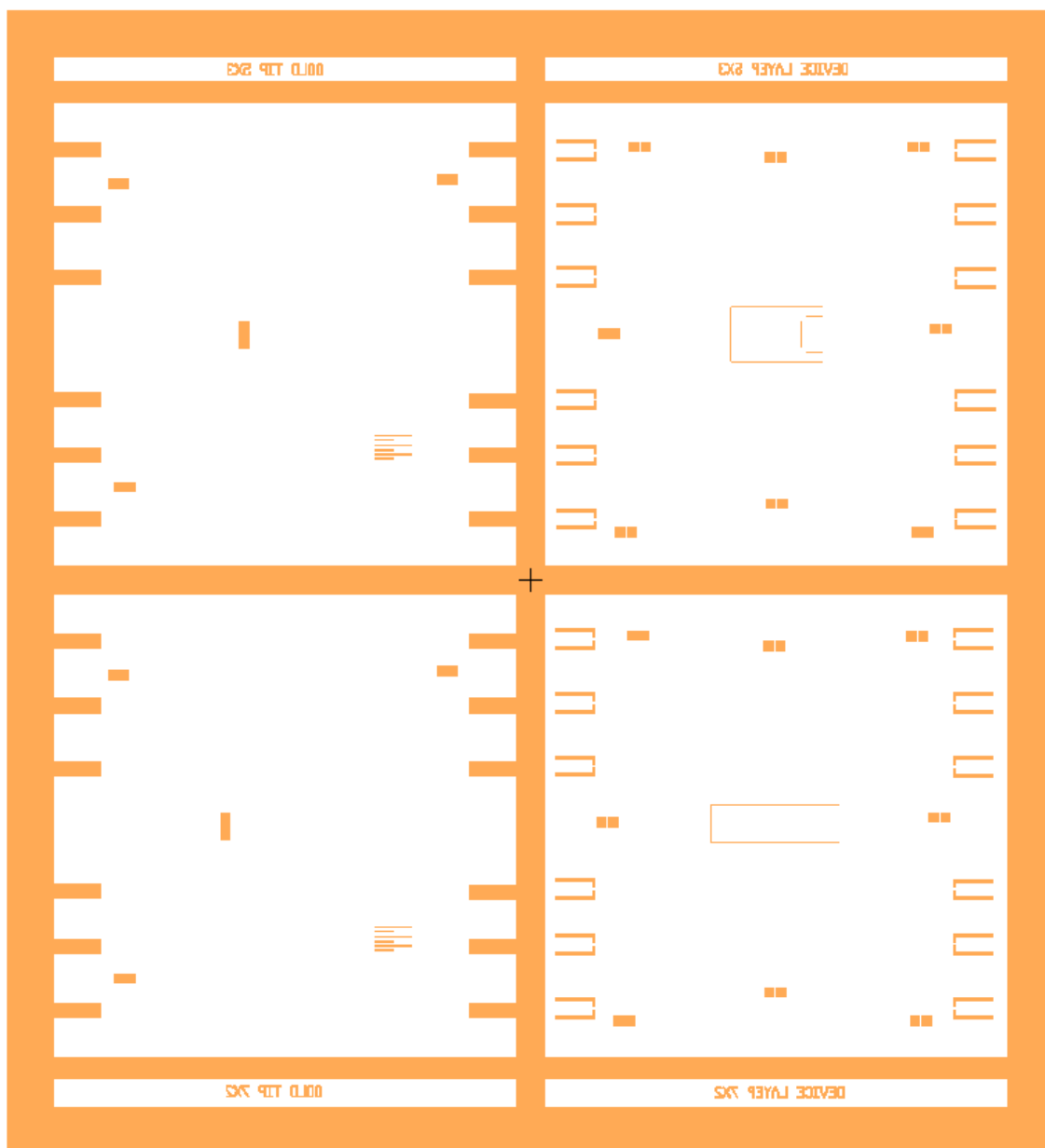
Figure 45. The gold (Au) tip and device layer mask. This single mask has 4 masks within it, masks for a Au spot and device layer for both a 5x3 mm^2 and a 7x2 mm^2 cantilever. The thickness of the beam is up to the user.

Figure 46. Zoomed view of the gold (Au) spot mask for a 7x2 mm^2 cantilever. The thickness of the beam is up to the user.
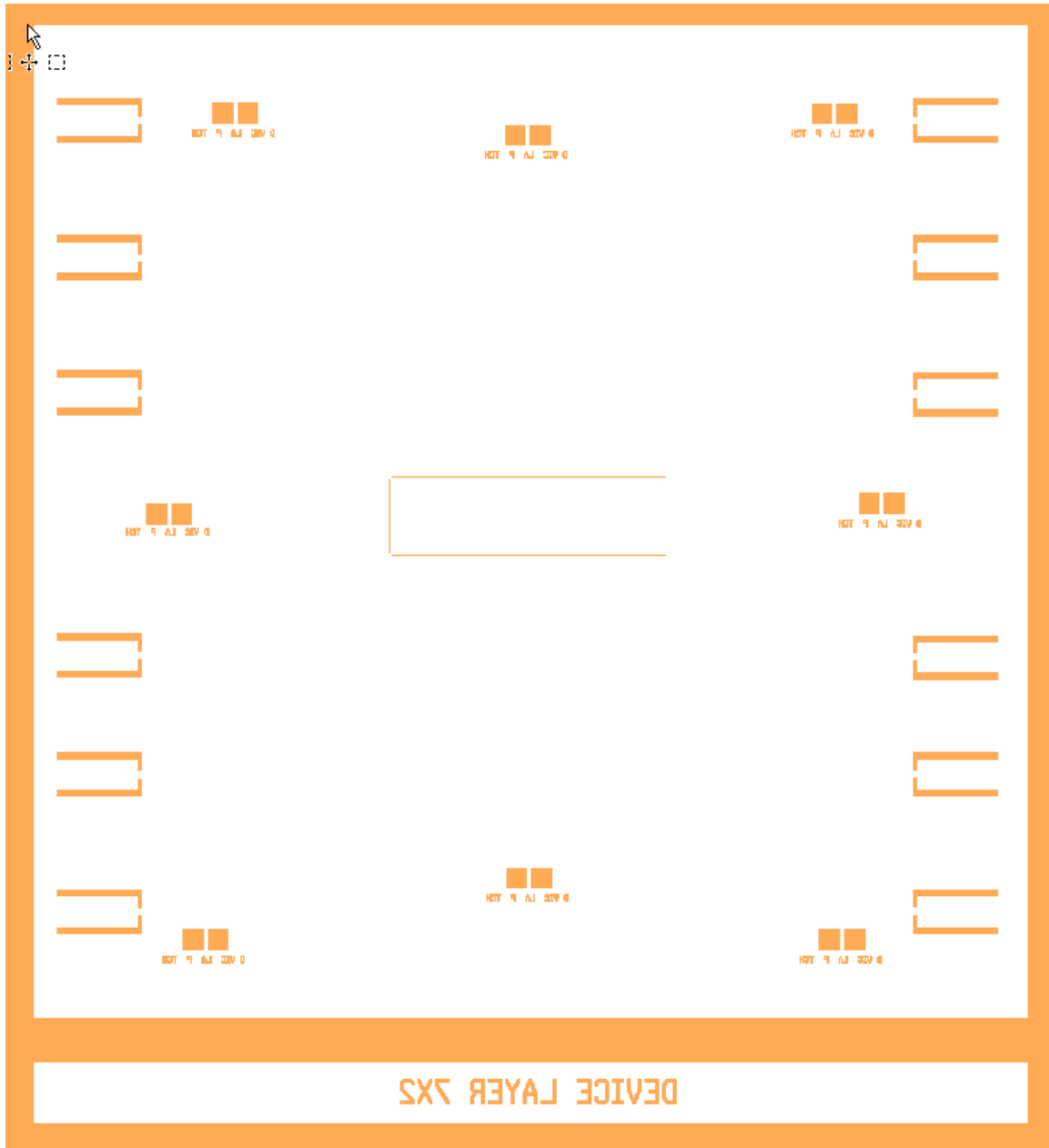
Figure 47. Zoomed view of the device layer mask for a 7x2 mm^2 cantilever. The thickness of the beam is up to the user.

The series of six rectangles on either side of mask shown in Figure 46 and the matching outline on either side of the mask in Figure 47 are the alignment marks used to align the device layer mask onto the sample that has already been exposed and developed using the gold tip mask. Shown in Figure 48 is a zoom view of the alignment marks used in the

previous two masks. These alignment marks are 10 µm across. Similar alignment marks exist in the backside mask shown in Figure 49.

Gold tip alignment marks

Device layer alignment marks

Figure 48. Zoom of the alignment marks at the edge of the rectangles shown in Figure 46 and their counterparts in Figure 47. These alignment marks are 10 µm across.
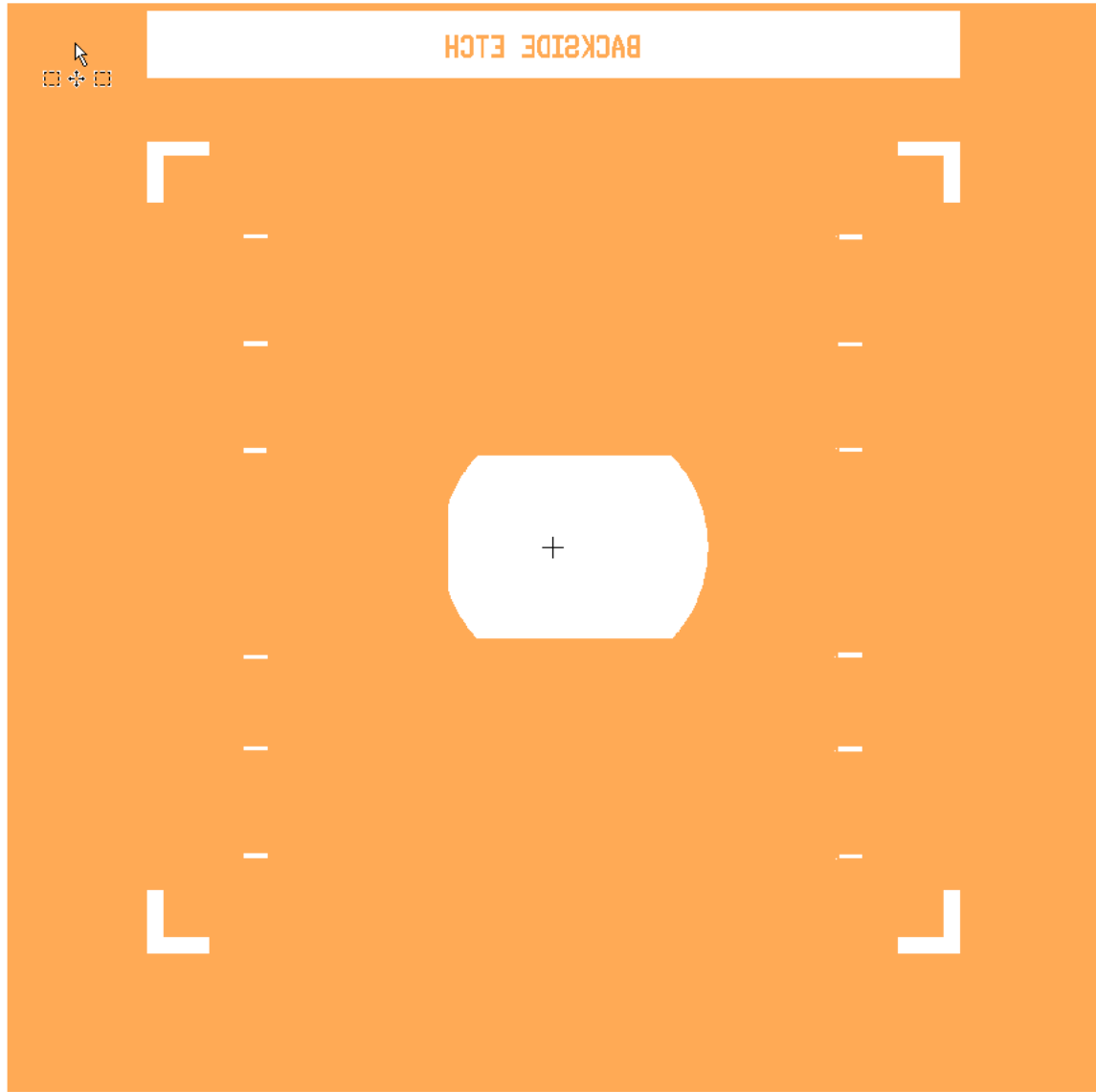
Figure 49. Backside etch mask for a 7x2 mm^2 cantilever. This mask is to be used in conjunction with a backside-mask aligner. The thickness of the beam is up to the user.

The exact process follower used to fabricate the cantilever in this research effort is shown below.

Process Follower for Cantilever Device

Overview of fabrication steps:

- Clean photoresist off device layer after dicing

- Deposit oxide layer

- Device layer Etch

- Backside DRIE etch

- Remove buried oxide

Clean photoresist off device layer after dicing

- With PR still on device layer, mark backside with diamond scribe with a "B" in one of the corners

- Clean sticky tape residue off after dicing with a cotton swab and acetone

- On the spinner, soak with acetone, then spray off with acetone pressure sprayer until clean, ~20 sec

- Standard clean for samples on the spinner

     Spinner settings – spread 20 sec on 500 RPM, spin 5 sec on 1,000 RPM;

- 25 sec Acetone
- 25 sec Methanol
- 25 sec Isopropyl

79

- 25 sec DI water
- Dry with N2 gun for full cycle of spinner
- Clean sample in plasma asher
    - 125 W for 3 minutes
- Bake on 200 °C hotplate for 5 min if applying another coat of PR
- Cool for longer than 2 min

Deposit oxide on device layer

-Grow Oxide in furnace to desired thickness and etch prior to processing

Device layer Etch

- For 5 and 10 um device layers
    - Coat sample with 1818, ramp set at 800, 3 sec on 500 RPM spread, 30 sec on 3,000 RPM spin.
    - Bake at 110 °C for 90 sec
    - Expose sample with Device mask on MJB3 for 8.2 sec.
    - Spray develop with 5:1 (DI:351) for 30 sec, holding the sample with a tweezers or on the spinner with vacuum, no spinning required
    - Rinse with DI for 30 sec
    - Dry with N2 for 30 sec
    - Bake at 110 °C for 20 min

    DRIE device layer

    - WPFAT
        ▪ Assume 7um/min etch rate +10% over etch
            • Very little effect on sample gap has been observed from over etching by even 3 minutes

    RIE device layer (Trion Etch Recipes.xlsx)

    - * * * Ensure etch director is positioned over the Si area to be etched
    - Run Si_SF6_ETCH
        o 200W
        o 100 mTorr

- o 30 sccm of SF6 and 3 sccm O2
    - 5um device layer – 92-101 sec (101 sec is 10% over etch)
    - 10um device layer – 184-202 sec (202 sec is 10% over etch)

- For 20 and 40 um device layers
    - Coat sample with AZ 9260, ramp set at 800, 3 sec on 500 RPM spread, 60 sec on 2,500 RPM spin.
    - Bake at 110 °C for 3 min (165 sec minimum)
    - Expose sample with Device mask on MJB3 for 2.16 min (need 1,500 mJ/cm^3).
    - Spray develop with 4:1 (DI:AZ400K) for 180-230 sec holding the sample with blue clamps, may have to go longer due to not using heated developer.
    - Rinse with DI for 20 sec
    - Dry with N2 for 30 sec
    - Bake at 90 °C for 30 min
    - DRIE etch for: (DRIE calculations.xlsx)
        - 20um device layer – 2.86-3 min (3 is 5% over etch)
        - 40um device layer – 5.71-6 min (6 is 5% over etch)

Backside Etch

- ** Ensure back side of handle wafer does not have an oxide layer on it before the SU-8 pattern is applied

- DRIE carrier wafer
    - Perform standard clean on 4 in wafer
    - Remove surface oxide with BOE
    - Rinse with DI water for 30 sec
    - Bake on 200 °C hotplate for 5 min
    - On the Suss spinner
        - Recipe 8 (settings on page 2 of notebook)
        - Dispense SU-8 2025 to cover ¾ of the wafer
        - Wipe off back of wafer with EBR
            - ** Back needs to be clean for DRIE Helium back side cooling
        - "Air-Bake" at room temperature for ~1 min
        - Pre-Bake @ **65 °C** for **3 min**, then move directly to second hotplate for soft-bake
        - Soft Bake @ **95 °C** for **6 min**
    - Expose on MAB-6 at AFRL
        - Remove mask holder

- Set to flood exposure
- Exposure time = 60 sec
- Post Exposure Bake (PEB)
  - PEB 1 @ **65 °C** for **3 min**, then move directly to second hotplate for PEB 2
  - PEB 2 @ **110 °C** for **10 min**, then move directly to **200 °C** covered hotplate or oven for **1-2 hours**

- SF-11 protective device layer coating
  - Perform standard clean on front and back of wafer while holding it with a tweezers, bake step important before SF-11 deposition
  - Coat device layer with SF11, ramp set at 800, 3 sec on 500 RPM spread, 45 sec on 3,000 RPM spin. Bake at 170 °C for 5min

- SU-8 25 coating at AFIT
  - Coat sample with ~1ml SU-8 25, ramp set at 800, 5 sec on 500 RPM spread, 30 sec on 2,800 RPM spin.   (3kRPM yields ~18 μm thick SU-8 which held up okay in the DRIE through the handle wafer)
    - "Air-Bake" at room temperature for ~1 min
    - Pre-Bake @ **65 °C** for **3 min**, then move directly to second hotplate for soft-bake
    - Soft Bake @ **95 °C** for **7 min**
  - Wrap samples in aluminum foil and take them to AFRL for Exposure, PEB, develop, and DRIE

  - Expose on MAB-6 at AFRL
    - Set alignment gap = ~80 μm
    - Set exposure time = 60 Sec
    - Exposure mode = Low Vac
      - Required dose is roughly 150-250 mJ/cm^2

      - Lamp power = _____
    - During back side alignment, shift over one alignment mark to the make the base of the cantilever be more released
  - Post Exposure Bake (PEB)
    - PEB 1 @ **65 °C** for **1 min**, then move directly to second hotplate for soft-bake
    - PEB 2 @ **95 °C** for **3 min**
  - Develop – **3-4 minutes**
    - Place sample in small dish, spray with SU-8 Developer until immersed in liquid. Puddle develop, spray occasionally. Rinse area with SU-8 Dev as sample is pulled out at 3-4 min mark

- o   Rinse with isopropyl alcohol (IPA) ~15 sec
- o   Rinse with DI water 30 sec
- o   Dry with N_2 gun 30 sec

- Hard bake
    - o   **65 °C** for **2 min**, then move directly to second hotplate for hard-bake
    - o   **95 °C** for **3 min**, increase temperature to **110 °C for ~1 hour or 130 °C for ~30 min**

DRIE

- Place a small drop of fomblin oil on the SU-8 carrier wafer, then place sample on oil spot. Ensure it is securely in place and doesn't slide away.
    - ▪   DRIE with WPFAT program in two etches for a total etch time of 55 min
        - •   Etch for 30 min, check samples and carrier for unwanted etch spots and apply Kapton tape as needed
        - •   Etch for additional 25 min
        - •   *** Membranes on samples are fragile now, apply IPA to carrier wafer and edges of samples.   As IPA cleans away oil, lightly push samples until they can float to the edge of the carrier wafer

- Remove SF-11
    - Set hotplate to 125 °C with PG remover in 50 ml beaker, soak sample for 30 min
    - Rinse off with IPA, dry with N2
    - Plasma ash for 3 min at 125 W
        - o   Put a glass slide in the Petri dish, set sample in dish partially on the slide to allow air to go under the sample

- 1818 protective device layer coating
    - Coat device layer with 1818, ramp set at 800, 3 sec on 500 RPM spread, 30 sec on 560 RPM spin.
    - Bake at 110 °C for 5min

- **RIE remaining silicon on backside**
    - Set up laser depth monitor over Si area
    - Etch through remaining backside silicone until cantilever is free
        - ▪   Aggressive etch first

- ▪ 100 mTorr
- ▪ 150 W
- When BOX becomes exposed, used gentle etch until cantilever is free
  - ▪ 150 mTorr
  - ▪ 100 W

** Very carefully remove sample from chamber **

Remove buried oxide

- Using blue locking claps, carefully clip onto sample without jarring it
  - ▪ Suspend sample over HF container for 5-7 minutes until BOX is gone
  - ▪ Dip in DI water
  - ▪ Dip sample into 50 ml beaker of acetone for 5-10 min
    - • Repeat with additional fresh beakers of acetone 2-3 more times
  - ▪ Pull sample out and allow to air dry

- Ash sample to clean off any remaining PR
  ** Caution ** – over time in the plasma asher, the sample heats up. If the SU-8 on

  the backside is undercut during the HF release, the SU-8 can bubble up and be

  removed too, which can cause the sample to move and potentially break the

  cantilever. Carefully remove any released SU-8 before the sample goes into the

  asher.

- Put a glass slide in the Petri dish, set sample in dish partially on the slide to allow air to go under the sample
- Ash for 1-3 min at 125 W, ash additional time is needed in 3 min segments

Appendix D. Matlab Code

The PA data collected in the LabView software was analyzed using a MATLAB®

script written by Major Nathan Glauvitz. Below is the script used to analyze and plot the

PA spectral data collected.

```matlab
%% Analysis PA Spectral Data
% reads data from *.txt file
clear all; close all; clc;
%% Enter radiation source power
power = 0.000025 % Power in watts
%% Enter absorption strength at for the strongest line
% Absorption coefficient in cm^-1 for
absorption_max = 0.053871
%% Enter the signal averaging time (sec)
averaging_time = 1;
%% Window sample size
window_size = 100
%% Description of Data file content
% Column 1 is not used
% Column 2 is the THz Diode excitation frequency, Loaded in THz from the file
% Column 3 is the Oscilliscope signal from the HeNe diode
% Column 4 is the THz Diode average voltage
% Column 5 is the lock-in Ampliphier signal (R)
[filename, pathname, filterindex] = uigetfile({ '*.*', 'All Files (*.*)'}, ...
'Select THz data files to process...', 'MultiSelect', 'on');
%% Loop over selected files, reading each into a data matrix
% Read in base pressure file first
B = [];
if ~iscell(filename) % handle single file selection
nFiles = 1;
filename = {filename};
else
nFiles = size(filename,2);
end
for i = 1:nFiles
178
fid = fopen(fullfile(pathname,char(filename(i))));
B = [B; textscan(fid, '%[^...] %f %f %f %f', 'delimiter', ' ', 'MultipleDelimsAsOne', 1)];
fclose(fid);
end
%% Plots the Oscilliscope signal
figure;
```

```matlab
axes2 = axes('Parent',gcf,'FontSize',24,'FontName','Times New Roman');
box(axes2,'on');
hold(axes2,'all');
hold on;
for i = 1:nFiles
hold on;
plot(1000*B{i,2},B{i,3}/1000,'g');
end
ylabel('PA Signal (a.u.)','FontSize',30,'FontName','Times New Roman')
xlabel('Frequency (GHz)','FontSize',30,'FontName','Times New Roman');
pf(1) = 4.5;
pf(2) = 14.5;
width = 40; % [cm]
height = 10; % [cm]
set(gcf,'Units','centimeters','Position',[pf(1) pf(2) width height]);
hold off;
%% Finds the variance over a window_size interval
dimension=size(B{1,5});
for i=1:dimension(1,1)-window_size
var1(i,1) = var(B{1,5}(i:i+window_size,1));
end
[o,p] = min(var1); % locates the index of minimum varience
for i=1:dimension(1,1)-window_size
var_THz(i,1) = var(B{1,4}(i:i+window_size,1));
end
figure;
axes2 = axes('Parent',gcf,'FontSize',24,'FontName','Times New Roman');
box(axes2,'on');
hold(axes2,'all');
plot(1000*B{1,2}(1:dimension(1,1)-window_size,1),var1);
hold on;
plot(1000*B{1,2}(1:dimension(1,1)-window_size,1),var_THz,'r');
ylabel('Variance','FontSize',30,'FontName','Times New Roman');
xlabel('Frequency (GHz)','FontSize',30,'FontName','Times New Roman');
pf(1) = 4.5;
179
pf(2) = 1.5;
width = 40; % [cm]
height = 10; % [cm]
set(gcf,'Units','centimeters','Position',[pf(1) pf(2) width height]);
hold off
%% Fluctuations in THz signal
for i=1:dimension(1,1)-1
THz_diode_fluctuations(i,1) = B{1,4}(i,1) - B{1,4}(i+1,1);
end
```

```matlab
Sig_fluct=abs(THz_diode_fluctuations);
THz_Fluctuation_mean=mean(sqrt(THz_diode_fluctuations.^2))
figure;
axes2 = axes('Parent',gcf,'FontSize',24,'FontName','Times New Roman');
box(axes2,'on');
hold(axes2,'all');
plot(1000*B{1,2}(1:dimension(1,1)-1,1),Sig_fluct);
hold on;
plot(1000*B{1,2}(1:dimension(1,1)-1,1),THz_Fluctuation_mean,'g','LineWidth',2.5);
ylabel('Mean Fluctuations in THz Diode Signal (V)','FontSize',30,'FontName','Times New Roman');
xlabel('Frequency (GHz)','FontSize',30,'FontName','Times New Roman');
pf(1) = 4.5;
pf(2) = 1.5;
width = 40; % [cm]
height = 25; % [cm]
set(gcf,'Units','centimeters','Position',[pf(1) pf(2) width height]);
hold off
%% Fluctuations in R-lock-in signal
for i=1:dimension(1,1)-1
R_signal_fluctuations(i,1) = B{1,5}(i,1) - B{1,5}(i+1,1);
end
R_Sig_fluct=abs(R_signal_fluctuations);
R_Fluctuation_mean=mean(sqrt(R_signal_fluctuations.^2))
figure;
axes2 = axes('Parent',gcf,'FontSize',24,'FontName','Times New Roman');
box(axes2,'on');
hold(axes2,'all');
plot(1000*B{1,2}(1:dimension(1,1)-1,1),R_Sig_fluct);
180
hold on;
plot(1000*B{1,2}(1:dimension(1,1)-1,1),R_Fluctuation_mean,'g','LineWidth',2.5);
ylabel('Mean Fluctuations in PA Signal (a.u.)','FontSize',30,'FontName','Times New Roman');
xlabel('Frequency (GHz)','FontSize',30,'FontName','Times New Roman');
pf(1) = 4.5;
pf(2) = 1.5;
width = 40; % [cm]
height = 25; % [cm]
set(gcf,'Units','centimeters','Position',[pf(1) pf(2) width height]);
hold off
%% find RMS noise floor of R-signal for window size interval
dimension=size(B{1,5});
for i=1:dimension(1,1)-window_size
RMS1(i,1) = sqrt(mean((B{1,5}(i:i+window_size,1)).^2));
```

```matlab
end
[o1,p1] = min(RMS1); % locates the index of minimum RMS noise
disp('Index start and frequency of lowest noise');
disp(p1)
disp(1000*B{1,2}(p1,1));
figure;
semilogy(1000*B{1,2}(1:dimension(1,1)-window_size,1),RMS1);
hold on;
semilogy(1000*B{1,2}(1:dimension(1,1)-window_size,1),var1,'r');
hold off;
RMS_noise = sqrt(mean((B{1,5}(p1:p1+window_size,1)).^2));
disp('RMS Noise Floor');
disp(RMS_noise);
Frequency1_of_noise_measured = 1000*B{1,2}(p1,1)
Frequency2_of_noise_measured = 1000*B{1,2}(p1+window_size,1)
Max_PA_signal = max(B{1,5});
disp('Max_PA_signal');
disp(Max_PA_signal);
SNR = Max_PA_signal / RMS_noise;
disp('SNR RMS_noise');
disp(SNR);
181
%% Sensitivity absorption_min
alfa_min = absorption_max / SNR;
disp('Sensitivity, alfa_min in cm^-1');
disp(alfa_min);
%% NNEA
NNEA = alfa_min * power * sqrt(averaging_time);
disp('NNEA, in cm^-1 W Hz^(-1/2)');
disp(NNEA);
%% Plots the "R" lock in signal
figure;
axes2 = axes('Parent',gcf,'FontSize',24,'FontName','Times New Roman');
box(axes2,'on');
hold(axes2,'all');
hold on;
for i = 1:nFiles
hold on;
array_size = ones(size(B{i,2}));
plot(1000*B{i,2},B{i,5},'b');
plot(1000*B{i,2},RMS_noise*array_size,'g')
end
ylabel('PA Signal (a.u.)','FontSize',30,'FontName','Times New Roman');
xlabel('Frequency (GHz)','FontSize',30,'FontName','Times New Roman');
pf(1) = 5;
```

```matlab
pf(2) = 2;
width = 40; % [cm]
height = 20; % [cm]
set(gcf,'Units','centimeters','Position',[pf(1) pf(2) width height]);
hold off;
%% Plots the THz detector average voltage
figure;
axes2 = axes('Parent',gcf,'FontSize',24,'FontName','Times New Roman');
box(axes2,'on');
hold(axes2,'all');
for i = 1:nFiles
hold on;
plot(1000*B{i,2},2*B{i,4},'k')
end
ylabel('THz Diode (V)','FontSize',30,'FontName','Times New Roman');
xlabel('Frequency (GHz)','FontSize',30,'FontName','Times New Roman');
182
pf(1) = 5;
pf(2) = 15;
width = 40; % [cm]
height = 10; % [cm]
set(gcf,'Units','centimeters','Position',[pf(1) pf(2) width height]);
hold off;
```

Below is a table of the simulations performed through CoventorWare® of varying cantilever dimensions. The shown values in green / yellow are the frequencies that the first 2 modal harmonics occur at. The tip displacement is the maximum displacement at the first modal harmonic.

Table 4. Modal analysis using 10 mPa for load pressure

DOE - Cantilever **Modal Resonant Frequency** for 10um thick Si						numbers from **25um** planar extrude in Z-10um bricks					
Width Length	1			2			3			5		
	Mode 1	Mode 2	Tip displacement (um)	Mode 1	Mode 2	Tip displacement (um)	Mode 1	Mode 2	Tip displacement (um)	Mode 1	Mode 2	Tip displacement (um)
3 (mesh parabolic)	1,516.63	8,542.32	0.0073	1,526.28	4,765.54	0.0072	1,527.36	3,500.80	0.0072			
5 (mesh parabolic)	549.92	3,445.98	0.0555	550.12	2,629.64	0.0555	550.25	1,869.13	0.0555	550.40	1,261.26	0.0555
7	280.67	1,758.70	0.2132	280.76	1,759.10	0.2130	280.93	1,264.61	0.2128	280.90	830.15	0.2129
9	169.83	1,064.09	0.5822	169.86	1,064.13	0.5820	169.91	953.96	0.5817	169.96	614.70	0.5815
10.00										137.65	543.53	0.89

Appendix F. Chamber Dimensions

Below is a rough sketch of half the chamber with all dimensions shown measured in inches. This is the back half of the chamber which houses the expansion volume. It is machined entirely out of a single block of stainless steel. The cantilever and 1x1 in^2 silicon handle sits on the right side of the block, in the recess.
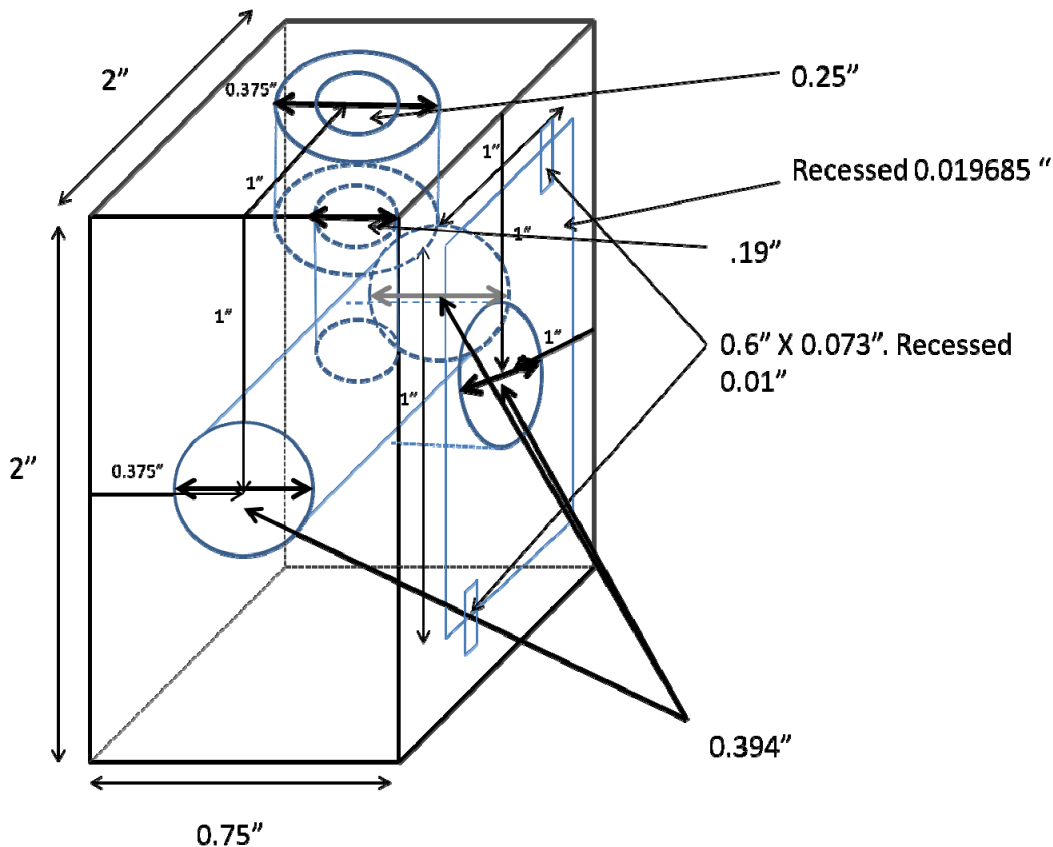

Figure 50. Drawing of the back half of the test chamber. This half of the chamber houses the expansion volume and is machined from a single block of stainless steel.

Bibliography

[1] T. Kuusela and J. Kauppinen, "Photoacoustic gas analysis using interferometric cantilever microphone," *Applied Spectroscopy Reviews,* vol. 42, no. 5, pp. 443-474, 2007.

[2] Summit Technical Media, LLC, "Terahertz (THz) Technology: An Introduction and Research Update," *High Frequency Electronics,* pp. 38-40, 2008.

[3] T. Kuusela, J. Peura, B. Matveev, M. Remennyy and N. Stus, "Photoacoustic gas detection using a cantilever microphone and III-V mid-IR LEDs," *Vibrational Spectroscopy 51,* pp. 289-293, 2009.

[4] G. A. West, J. J. Barrett, D. R. Siebert and K. Virupaksha Reddy, "Photoacoustic spectroscopy," *Rev. Sci. Instrum. 54,* pp. 797-817, 1983.

[5] A. G. Bell, "Upon the production of sound by radiant energy," *Philosophical Magazine,* vol. 11, pp. 510-528, 1881.

[6] A. Garcia-Valenzuela and J. Villatoro, "Noise in optical measurements of cantilever deflections," *J. Appl. Phys.,* vol. 84, no. 1, pp. 58 - 63, 1998.

[7] C. H. Townes and S. Geschwind, "Limiting sensitivity of a microwave spectrometer," *J. Appl. Phys.,* vol. 19, no. 8, pp. 795 - 796, 1948.

[8] K. B. Lee, Principles of Microelectromechanical Systems, Hoboken, New Jersey: John Wiley & Sons, Inc, 2011.

[9] J. W. Judy, "Microelectromechanical systems (MEMS): fabrication, design and applications," *Smart Materials and Structures,* pp. 1115-1134, 2001.

[10] F. Laermer and A. Schilp, "Method of anisotropically etching silicon". Patent 5,501,893, 1996.

[11] M. K. Hooda, M. Wadhwa, S. Verma, M. M. Nayak, P. J. George and A. K. Paul, "A systematic study of DRIE process for high aspect ratio microstructuring," *Vacuum,* vol. 84, no. 9, pp. 1142 - 1148, 2010.

[12] S.-O. Choi, S. Rajaraman, Y.-K. Yoon, X. Wu and M. G. Allen, "3-D PATTERNED MICROSTRUCTURES USING INCLINED UV EXPOSURE," *Proc. of Solid State Sensors, Actuators, and Microsystems Workshop,* pp. 348 - 351, 2006.

[13] B. Olbrechts and J. Raskin, "PECVD oxide as intermediate film for wafer bonding: Impact of residual stress," *Microelectronic Engineering,* vol. 87, no. 11, pp. 2178 - 2186, 2010.

[14] G. K. Celler and S. Cristoloveanu, "Frontiers of silicon-on-insulator," *Journal of Applied Physics,* vol. 93, no. 9, pp. 4955-4978, 2003.

[15] G. Bajor and J. Raby, "Using a rapid thermal process for manufacturing a wafer bonded soi semiconductor". United States of America Patent 4,771,016, 24 April 1987.

[16] A. Miklos, P. Hess and Z. Bozoki, "Application of acoustic resonators in photoacoustic trace gas analysis and metrology," *Review of Scientific Instruments,* vol. 72, no. 4, pp. 1937-1955, 2001.

[17] J. Kauppinen, K. Wilcken, I. Kauppinen and V. Koskinen, "High sensitivity in gas analysis with photoacoustic detection," *Microchemical Journal,* vol. 76, pp. 151-159, 2004.

[18] J. Fonsen, V. Koskinen, K. Roth and J. Kauppinen, "Dual cantilever enhanced photoacoustic detector with pulsed broadband IR-source," *Vibrational Spectroscopy,* pp. 214-217, 2008.

[19] M. De Paula, A. A. De Carvalho, C. A. Vinha, N. Cella and H. Vargas, "Optical microphone for photoacoustic spectroscopy," *J. Appl. Physs,* pp. 3722-3724, 1988.

[20] N. Ledermann, P. Muralt, J. Baborowski, M. Forster and J.-P. Pellaux, "Piezoelectric pb(zr x, ti 1-x) O 3 thin film cantilever and bridge acoustic sensors for miniaturized photoacoustic gas detectors.," *Journal of Micromechanics and Microengineering,* pp. 1650 - 1658, 2004.

[21] P. Sievila, V.-P. Rytkonen, O. Hahtela, N. Chekurov, J. Kauppinen and I. Tittonen, "Fabrication and characterization of an ultrasensitive acouto-optical cantilever," *Journal of Micromechanics and Microengineering,* pp. 852-859, 2007.

[22] P. Sievila, N. Chekurov, J. Raittila and I. Tittonen, "Sensitivity-improved cantilever microphone for acousto-optical detection," *Sensors and Actuators A: Physica,* pp. 90-95, 2012.

[23] K. Biswas and S. Kal, "Etch characteristics of KOG, TMAH and dual doped TMAH for bulk micromachining of silicon," *Microelectron. J.,* vol. 37, no. 6, pp. 519 - 525, 2006.

[24] "JPL molecular spectroscopy catalog," [Online]. Available: http://spec.jpl.nasa.gov/.

[25] N. Glauvitz, "MEMS Cantilever Sensor For THz Photoacoustic Chemical Sensing and Spectroscopy (Unpublished doctoral dissertation)," *Air Force Institute of Technology, WPAFB, OH,* 2013.

[26] E. J. Boyd and D. Uttamchandani, "Measurement of the anisotropy of young's modulus in single-crystal silicon," *Microelectromechanical Systems, Journal of,* vol. 21, no. 1, pp. 253 - 249, 2012.

[27] J. Dundurs and M. S. Lee, "Stress concentration at a sharp edge in contact problems," *Journal of Elasticity,* vol. 2, no. 2, pp. 109-112, 1972.

[28] K. Fukunaga, I. Hosako, Y. Ogawa and S. Hayashi, "Terahertz spectroscopy for art conservation," *IEICE Electronics Express,* vol. 4, no. 8, pp. 258-263, 2007.

[29] N. Glauvitz, S. Glazevic, R. Coutu, Jr., M. Kistler, I. R. Medvedev and D. Petkie, "A MEMS photoacoustic detector of terhaertz radiation for chemical sensing," *Proc. Eurosensors XXVI,* pp. 730 - 733, 2012.

[30] S. S. Lee and R. M. White, "Self-excited piezoelectric cantilever oscillators," *Sensors and Acuators,* pp. 41-45, 1996.

[31] N. Glauvitz, R. Coutu, Jr., M. Kistler, I. R. Medvedev and D. Petkie, "MEMS cantilever sensor for photoacoustic detection of terahertz radiation," in *SEM 2013 Annual Conference & Exposition on Experimental and Applied Mechanics*, Lonbard, IL, 2013.

[32] J. Peltola, M. Vainio, T. Hieta, J. Uotila, S. Sinisalo, M. Metsala, M. Siltanen and L. Halonen, "High sensitivity trace gas detection by cantilever-enhanced photoacoustic spectroscopy using a mid-infrared continuous-wave optical

parametric oscillator," *Opt. Express,* vol. 21, no. 8, pp. 10240-10250, 2013.

[33] B. Adamson, J. Sader and E. Bieske, "Photoacoustic detection of gases using microcantilevers," *J. Appl. :hys.,* vol. 106, p. 114510, 2009.

[34] D. K. DeVoe and A. P. Pisano, "Modeling and Optimal Design of Piezoelectric Cantilever Microactuators," *Journal of Microelectromechanical Systems,* vol. 6, no. 3, pp. 266 - 270, 1997.

[35] R. D. Cook, D. S. Malkus, M. E. Plesha and R. J. Witt, Concepts and Applications of Finite Element Analysis, United States: John Wiley & Sons, Inc., 2002.

[36] CoventorWare Analyzer Reference, Cary NC: Coventor Inc., 2010.

[37] A. Rosencwaig, Photoacoustics and Photoacoustic Spectroscopy, New York: John Wiley & Sons Inc., 1980.

[38] A. Ariyoshi, C. Otani, A. Dobroiu, H. Matsuo, H. Sato, T. Taino, K. Kawase and H. M. Shimizu, "Superconducting Detector Array for Terahertz Imaging Applications," *Japanese Journal of Applied Physics,* vol. 45, pp. L1004 - L1006, 2006.

[39] H. Tao, E. A. Kadlec, A. C. Strikwerda, K. Fan, W. J. Padilla, R. D. Averitt, E. A. Shaner and X. Zhang, "Microwave and terahertz wave sensing with metamaterials," *Opt. Express,* vol. 19, no. 22, pp. 21620 - 21626, 2011.

[40] S. Chen, Y. Choe, K. Baumgartel, A. Lin and S. E. Kim, "Edge-released, piezoelectric MEMS acoustic transducers in array configuration," *Journal of Micromechanics and Microengineering,* vol. 22, no. 2, pp. 1247 - 1250, 1991.

[41] A. Hulanicki, S. Glab and F. Ingman, "Chemical Sensors Definitions and Classifications," *Pure & Appl. Chem.,* vol. 63, no. 9, pp. 1247 - 1250, 1991.

[42] A. Mandelis, Principles & Perspectives of Photothermal & Photoacoustic Phenomena, New York: Elsevier Science Publishing Co. Inc., 1992.

[43] S. L. Dexheimer, Terahertz Spectroscopy, Boca Raton: CRC Press, 2008.

[44] J. U. White and N. L. Alpert, "Wide range infrared absorption cell," *J. Opt. Soc. Am.,* vol. 47, no. 5, pp. 460 - 462, 1958.

[45] R. G. Pilston and J. U. White, "A long path gas absorption cell," *J. Opt. Soc. Am.,* vol. 44, no. 7, pp. 572 - 572, 1954.

[46] J. Parasuraman, A. Summanwar, F. Marty, P. Basset, D. E. Angelescu and T. Bourouina, "Deep reactive ion etching of sub-micrometer trenches with ultra high aspect ratio," *Microelectronic Engineering,* vol. 113, no. 0, pp. 35 - 39, 2014.

[47] V. Cracium, J. Elders, J. G. Gardeniers and I. W. Boyd, "Characteristics of high quality ZnO thin films deposited by pulsed laser deposition," *Applied Physics Letters,* vol. 65, no. 23, pp. 2963 - 2965, 1994.

[48] S. Venkatachalam and Y. Kanno, "Preparation and characterization of nano and microcrystalline ZnO thin films by PLD," *Current Applied Physics,* vol. 9, no. 6, pp. 1232 - 1236, 2009.

[49] Z. Bi, Z. Zhang and P. Fan, "Characterization of PZT ferroelectric thin films by RF-magnetron sputtering," *International Conference on Nanoscience and Technology, Journal of Physics: Conference Series,* vol. 61, pp. 120 - 124, 2006.

[50] Z. Bi, Z. Zhang and P. Fan, "Effect of sputter deposition parameters on the characteristics of PZT ferroelectric thin films," *Internation Conference on Nanoscience and Technology, Journal of Physics: Conference Series,* vol. 61, pp. 115 - 119, 2006.

[51] T. Haccart, E. Cattan and D. Remiens, "Dielectric, ferroelectric and piezoelectric properties of sputtered PZT thin films on Si substrates: influence of film thickness and orientation," *Semiconductor Physics, Quantum Electronics & Optoelectronics,* vol. 5, pp. 78 - 88, 2002.

[52] K. Kakimoto, H. Ohsato, H. Kakemoto and Y. Masuda, "Stoichiometry and crystal orientation of YAG-PLD derived ferroelectric PZT thin film," *Journal of the European Ceramic Society,* vol. 24, no. 6, pp. 993 - 997, 2004.

[53] Q. Wang, X. Du, B. Xu and L. E. Cross, "Theoretical analysis of the sensor effect of cantilever piezoelectric benders," *J. Appl. Phys.,* vol. 85, no. 3, pp. 1702 - 1712,

1999.

[54] C. Lee, T. Itoh and T. Suga, "Self-excited piezoelectric PZT microcantilevers for dynamic SFM-with inherent sensing and actuating capabilities," *Sensors and Acuators A: Physical,* vol. 72, no. 2, pp. 179 - 188, 1999.

[55] C. Lee, T. Itoh and T. Suga, "Micromachined piezoelectric force sensors based on PZT thin films," *IEEE Transactions on Ultrasonics, Ferroelectrics, and Frequency Control,* vol. 43, no. 4, pp. 553 - 559, 1996.

[56] E. McNaghten, K. Grant, A. Parkes and P. Martin, "Simultaneous detection of trace gases using multiplexed tunable diode lasers and a photoacoustic cell containing a cantilever microphone," *Applied Physics B: Lasers and Optics,* vol. 107, no. 3, pp. 861 - 871, 2012.

[57] V. Koskinen, J. Fonsen, K. Roth and J. Kauppinen, "Cantilever enhanced photoacoustic detection of carbon dioxide using a tunable diode laser source," *Applied Physics B: Lasers and Optics,* vol. 86, no. 3, pp. 451 - 454, 2007.

[58] M. Hippler, C. Mohr, K. A. Keen and E. D. McNaghten, "Cavity-enhanced resonant photoacoustic spectroscopy with optical feedback cw diode lasers: A novel technique for ultratrace gas analysis and high-resolution spectroscopy," *J. Chem. Phys.,* vol. 133, no. 4, pp. 044308 (1 - 8), 2010.

[59] A. A. Kosterev, Y. A. Bakhirkin, R. F. Curl and F. K. Tittel, "Quartz-enhanced photoacoustic spectroscopy," *Opt. Lett.,* vol. 27, pp. 1902 - 1904, 2002.

[60] S. Borri, P. Patimisco, A. Sampaolo, H. E. Beere, D. A. Ritchie, M. S. Vitiello, G. Scamarcio and V. Spagnolo, "Terahertz quartx enhanced photo-acoustic sensor," *Appl. Phys. Lett.,* vol. 103, no. 2, pp. 021105 (1 - 4), 2013.

[61] J. Besson, S. Schilt and L. Thevenaz, "Multi-gas sensing based on photoacoustic spectroscopy using tunable laser diodes," *Spectrochimica Acta Part A: Molecular and Biomolecular Spectroscopy,* vol. 7, no. 10, pp. 2389 - 2401, 2004.

[62] Y. Wang, C. Lee and C. Chiang, "A MEMS-based air flow sensor with a free-standing micro-cantilever structure," *Sensors,* vol. 7, no. 10, pp. 2389 - 2401, 2007.

[63] Y. S. Kim, H. J. Nam, S. M. Cho, D. C. Kim and J. U. Bu, "A self-actuating PZT cantilever integrated with piezoresistor sensor for AFM with high speed parallel operation," *Fifteenth IEEE International Conference Micro Electro Mechanical Systems,* pp. 689 - 692, 2002.

[64] V. Koskinen, J. Fonsen, J. Kauppinen and I. Kauppinen, "Extremely sensitive trace gas analysis with modern photoacoustic spectroscopy," *Vibrational Spectroscopy,* vol. 42, no. 2, pp. 239 - 242, 2006.

[65] V. Koskinen, J. Fonsen, K. Roth and J. Kauppinen, "Progress in cantilever enhanced photoacoustic spectroscopy," *Vibrational Spectroscopy,* vol. 48, no. 1, pp. 16 - 21, 2008.

[66] C. B. Hirschmann, S. Sinisalo, J. Uotila, S. Ojala and R. L. Keiski, "Trace gas detection of benzene, toluene, p-, m- and o-xylene with a compact measurement system using cantilever enhanced photoacoustic spectroscopy and optical parametric oscillator," *Vibrational Spectroscopy,* vol. 23, no. 1, pp. 170 - 176, 2013.

[67] C. Haisch, "Photoacoustic spectroscopy for analytical measurements," *Measurement Science and Technology,* vol. 23, no. 1, pp. 012001 (1 - 17), 2012.

Vita

Richard A. Newberry was born in 1990 and is from San Antonio, Texas. He graduated from the United States Air Force Academy in 2012 with a BS degree in computer engineering. He is currently a graduate student at the Air Force Institute of Technology working on his MS in electrical engineering, working in the Microelectromechanical Systems (MEMS) group. His current degree focuses on the design and fabrication of a MEMS cantilever for trace gas detection.

1. REPORT DATE (DD-MM-YYYY) 27-03-2014	2. REPORT TYPE Master's Thesis	3. DATES COVERED (From – To) Aug 2012–Mar 2014

TITLE AND SUBTITLE	5a. CONTRACT NUMBER
Microelectromechanical Systems (MEMS) Photoacoustic (PA) Detector of Terahertz (THz) Radiation for Chemical Sensing	5b. GRANT NUMBER
	5c. PROGRAM ELEMENT NUMBER

6. AUTHOR(S)	5d. PROJECT NUMBER
Newberry, Richard, A, 2nd LT, USAF	5e. TASK NUMBER
	5f. WORK UNIT NUMBER

7. PERFORMING ORGANIZATION NAMES(S) AND ADDRESS(S) Air Force Institute of Technology Graduate School of Engineering and Management (AFIT/ENY) 2950 Hobson Way, Building 640 WPAFB OH 45433-8865	8. PERFORMING ORGANIZATION REPORT NUMBER AFIT-ENG-14-M-58

9. SPONSORING/MONITORING AGENCY NAME(S) AND ADDRESS(ES) Dr. Gernot Pomrenke gernot.pomrenke@us.af.mil Air Force Office of Scientific Research 875 N Randolph St, Ste 325 Rm 3112 Arlington AFB, VA 22203	10. SPONSOR/MONITOR'S ACRONYM(S) AFOSR
	11. SPONSOR/MONITOR'S REPORT NUMBER(S)

12. DISTRIBUTION/AVAILABILITY STATEMENT
DISTRUBTION STATEMENT A. APPROVED FOR PUBLIC RELEASE; DISTRIBUTION UNLIMITED.

13. SUPPLEMENTARY NOTES
This material is declared a work of the U.S. Government and is not subject to copyright protection in the United States.

14. ABSTRACT
In this research effort, a Microelectromechanical system (MEMS) cantilever pressure sensor was designed, modeled, and fabricated to investigate the photoacoustic (PA) response of gases to terahertz (THz) radiation under low vacuum conditions. Previous efforts in this project were improved upon, to include lowering resting out-of-plane curvature to improve sensitivity of devices. Dimensional analysis is taken into consideration and altered dimensions also serve to boost sensitivity while improving fragility of devices. All devices were fabricated on silicon-on-insulator (SOI) wafers and tested in a custom designed THz vacuum chamber. Fabricated devices have a minimum normalized noise equivalent absorption (NNEA) coefficient of 4.28×10^{-10}, an improvement of 69% on prior 10µm devices.

15. SUBJECT TERMS
MEMS, cantilevers, spectroscopy, terahertz, photoacoustic, chemical sensor

16. SECURITY CLASSIFICATION OF:			17. LIMITATION OF ABSTRACT	18. NUMBER OF PAGES	19a. NAME OF RESPONSIBLE PERSON Dr. Ronald A Coutu, Jr., AFIT/ENG
a. REPORT U	b. ABSTRACT U	c. THIS PAGE U	UU	117	19b. TELEPHONE NUMBER (Include area code) (937) 255-3636, ext 7230 ronald.coutu@afit.edu

Standard Form 298 (Rev. 8-98)
Prescribed by ANSI Std. Z39-18